Progress in Oceanography 122 (2014) 30–53

Contents lists available at ScienceDirect

Progress in Oceanography

journal homepage: www.elsevier.com/locate/pocean

Connections between physical, optical and biogeochemical processes in the Pacific Ocean

Peng Xiu *, Fei Chai

School of Marine Sciences, University of Maine, Orono, ME 04469, USA

ARTICLE INFO

Article history:
Received 1 January 2013
Received in revised form 19 November 2013
Accepted 25 November 2013
Available online 6 December 2013

ABSTRACT

A new biogeochemical model has been developed and coupled to a three-dimensional physical model in the Pacific Ocean. With the explicitly represented dissolved organic pools, this new model is able to link key biogeochemical processes with optical processes. Model validation against satellite and in situ data indicates the model is robust in reproducing general biogeochemical and optical features. Colored dissolved organic matter (CDOM) has been suggested to play an important role in regulating underwater light field. With the coupled model, physical and biological regulations of CDOM in the euphotic zone are analyzed. Model results indicate seasonal variability of CDOM is mostly determined by biological processes, while the importance of physical regulation manifests in the annual mean terms. Without CDOM attenuating light, modeled depth-integrated primary production is about 10% higher than the control run when averaged over the entire basin, while this discrepancy is highly variable in space with magnitudes reaching higher than 100% in some locations. With CDOM dynamics integrated in physical-biological interactions, a new mechanism by which physical processes affect biological processes is suggested, namely, physical transport of CDOM changes water optical properties, which can further modify underwater light field and subsequently affect the distribution of phytoplankton chlorophyll. This mechanism tends to occur in the entire Pacific basin but with strong spatial variability, implying the importance of including optical processes in the coupled physical-biogeochemical model.

1. Introduction

Light distribution below the ocean surface has been treated as a control mechanism for autotrophic growth. Optical and biogeochemical processes are essentially connected via the interaction of light with particulate and/or dissolved matters in the ocean. Under a given oceanic environment with ample nutrients, photosynthetic organism biomass generally increases with increasing light. As the biomass grows and accumulates, light absorption and scattering become stronger, leading to less light penetration in the water, which in turn provides a negative feedback for the biological activities (Yentsch and Phinney, 1989; Bissett et al., 2001; Rothstein et al., 2006). The impacts of physical processes on biogeochemical processes have been primarily recognized as horizontal and/or vertical transports of nutrients and plankton biomass. Changes in optical properties through physical processes, which alter underwater light field and further change biological activities, however, are another linkage between physical and biogeochemical processes. Thus, it is important to relate these processes when assessing marine ecosystem.

Many marine ecosystem models, varying from simple nutrient, phytoplankton, zooplankton, and detritus (NPZD) models to complex models with 20 or more components (e.g., Chai et al., 2002; Moore et al., 2002; Anderson and Pondaven, 2003; Aumont et al., 2003; Fennel et al., 2003; Goebel et al., 2010) often use an approximation of integrated photosynthetically active radiation (PAR, 400–700 nm) that only attenuates with phytoplankton biomass (or chlorophyll) and seawater to control the assimilation of inorganic nutrients. Such a simplification in relationship between light attenuation and phytoplankton biomass is easy to implement for numerical calculation and biological consideration. However, considerable nonlinearity exists when considering phytoplankton sizes and their photo-adaptive states (Smith and Baker, 1978; Bricaud et al., 1983). In addition to phytoplankton, detritus and colored dissolved organic matter (CDOM) absorption and particulate backscattering, referred to as inherent optical properties that are often not represented in ecosystem models can affect underwater light field as well (e.g., Babin et al., 2003a;Boss et al., 2004).

Adding optics to an ecosystem model has been suggested to be more accurate in generating subsurface light field (Fujii et al., 2007). Directly comparing modeled optical properties with ocean color and in situ data also gives additional constraints on model parameters to reduce uncertainties in model simulations, as many satellite-derived products, such as chlorophyll concentration,

* Corresponding author. Address: School of Marine Sciences, University of Maine 5706 Aubert Hall, Orono, ME 04469, USA. Tel.: +1 207 5814349.
E-mail address: peng.xiu@maine.edu (P. Xiu).

0079-6611/$ - see front matter © 2013 Elsevier Ltd. All rights reserved.
http://dx.doi.org/10.1016/j.pocean.2013.11.008

carbon biomass, and primary production, are estimated based on empirical or semi-analytical algorithms linking with ocean optics (IOCCG, 2006). However, only few ecosystem models have considered the optical processes associated with underwater light field (e.g., Bissett et al., 1999a; Fujii et al., 2007). The one-dimensional (1-D) ecosystem model developed by Fujii et al. (2007) is able to simulate underwater light field and the feedbacks to biological processes. The CDOM that is not included in their model, however, may have an important role in regulating phytoplankton dynamics and nutrient cycling in the euphotic zone. The production and destruction mechanisms for CDOM include phytoplankton exudation, zooplankton messy feeding, detritus breakdown, bacterial production and consumption, and photolysis by ultraviolet (UV, 280–400 nm) light, which are fundamentally different and decoupled from those for phytoplankton, especially in coastal regions where terrestrial CDOM is introduced. To incorporate CDOM in an ecosystem model, one must consider the cycling of dissolved matter pool and the microbial loop in the ocean in addition to the classic NPZD processes.

The objective of this study is to develop an ecosystem model that explicitly describes wavelength-resolved optical properties (visible light, 400–700 nm), associated with multi-nutrient phytoplankton, zooplankton, and detritus. We also include the photoacclimation process for phytoplankton in the model to better resolve the dynamic link between phytoplankton chlorophyll and carbon biomass. Carbonate system, including dynamics of total alkalinity, ocean calcification and the air-sea gas exchange of carbon dioxide, is explicitly represented as well. We couple this model to the Pacific Ocean (45°S to 65°N, 100°E to 70°W) with a three-dimensional (3-D) general circulation model. The model performance is examined by comparing model outputs with available satellite and in situ data. Numerical experiments are conducted to understand the dynamic connections between physical, optical and biogeochemical processes in the Pacific Ocean.

2. Model and data

2.1. Biogeochemical processes

The ecosystem model is primarily based on the Carbon, Silicon, Nitrogen Ecosystem (CoSINE) model (Chai et al., 2002). We follow previous approaches to simulate phytoplanktonic photo-acclimation and the dynamic chlorophyll-to-carbon ratio under different growth conditions (Geider et al., 1998; Moore et al., 2002; Fujii et al., 2007). The ecosystem consists of 31 state variables describing three phytoplankton functional groups in three different biomass forms, picoplankton nitrogen, carbon and chlorophyll (P1, C1, Chl1), diatoms nitrogen, carbon and chlorophyll (P2, C2, Chl2), and coccolithophorids nitrogen, carbon and chlorophyll (P3, C3, Chl3); two size classes of zooplankton, microzooplankton nitrogen (Z1), mesozooplankton nitrogen (Z2), and their carbon terms (ZC1, ZC2); detritus in terms of particulate organic nitrogen (PON), particulate organic carbon (POC), particulate inorganic carbon (PIC) and biogenic silica ($bSiO_2$); silicate ($Si(OH)_4$); phosphate (PO_4); dissolved oxygen (DO); total alkalinity (TALK); total CO_2 (TCO_2); two forms of dissolved inorganic nitrogen, nitrate (NO_3) and ammonium (NH_4); bacteria nitrogen (BAC); as well as dissolved organic matter, labile dissolved organic nitrogen (LDON), labile dissolved organic carbon (LDOC), colored labile dissolved organic carbon (CLDOC), semi-labile dissolved organic nitrogen (SDON), semi-labile dissolved organic carbon (SDOC), and colored semi-labile dissolved organic carbon (CSDOC) (Fig. 1). The governing equations and formulations of biogeochemical processes are denoted in Appendix A, and a list of parameters used in the model is provided in Table 1.

Nutrient uptake and photosynthetic rate are modeled as functions of environmental factors and cellular composition (C:Chl and C:N). The model includes down-regulation of pigment content at high irradiance or when growth rate is limited by nutrients and temperature, and feedback between nitrogen and carbon metabolism (Geider et al., 1998). Phytoplankton ratios (C:Chl and C:N) vary dynamically between maximum and minimum cell quotas according to the changes in light and nutrient levels (Xiu and Chai, 2012). The maximum and minimum cell quotas for different phytoplankton functional groups are chosen based on Moore et al. (2002) and Fujii et al. (2007).

All phytoplankton take up NO_3, NH_4, PO_4 and TCO_2 for photosynthesis. Diatoms also take up $Si(OH)_4$ for the silicification process, and coccolithophorids utilize TALK and TCO_2 for the calcification process (Fujii and Chai, 2007). The microzooplankton graze on picoplankton and bacteria. The mesozooplankton feed on diatoms, coccolithophorids, microzooplankton, and detritus. The remineralization of organic nitrogen, silicon and carbon, both inside and below the euphotic zone, is a critical process for nutrient recycling efficiency. It depends on a number of factors, including water temperature, nutrient condition, particle sizes and zooplankton grazing (Ragueneau et al., 2000; Ward, 2000). The remineralization of organic nitrogen is primarily biological with a rapid production of NH_4 and TCO_2 through zooplankton grazing in the euphotic zone and bacteria decomposition of organic matter below the euphotic zone. Below the euphotic zone, sinking particulate organic matter (POM) is converted to inorganic nutrients and dissolved organic matter (DOM) by a regeneration process. Through the dissolution process, a majority of the POM is converted to inorganic nutrients (90%), and the rest goes into the DOM pool.

The DOM pool consists of dissolved organic carbon and nitrogen. There are a number of processes that can produce and utilize or remineralize DOM, and most of these processes are poorly understood (Christian and Anderson, 2002). To the first-order approximation, DOM processes are modeled as consumption by bacteria and productions by phytoplankton exudation, zooplankton messy feeding, and detrital breakdown, as adopted in many studies (e.g., Anderson and Williams, 1998; Walsh et al., 1999; Tian et al., 2000; Christian and Anderson, 2002; Anderson and Pondaven, 2003). Phytoplankton exudation representing an active release by phytoplankton is modeled as a fraction of primary production. This fraction is highly variable in different studies, with magnitudes ranging from 2% to 56.4% (Christian and Anderson, 2002). Grazer-related DOM production is modeled as zooplankton messy feeding, which is a fixed fraction of grazed materials. Among previous studies, this fraction also varies significantly with a range of 2.5–50% (Christian and Anderson, 2002). From lab experiments, Strom et al. (1997) estimated that about 16–37% of algal carbon was released during an ingestion event. Particle dissolution into the DOM pool with the first-order rate process is used in our model. This approach is a simplified simulation of the underlying mechanism and has been widely used (e.g., Anderson and Williams, 1998; Levy et al., 1998; Vallino, 2000; Yamanaka et al., 2004), although other environmental factors such as temperature, turbulence, and bacteria can modify this process.

The primary mechanism for DOM loss is uptake by heterotrophic bacteria. According to different turnover rates, the DOM is further divided into labile and semi-labile pools. Labile pool can be consumed directly by bacteria, while semi-labile pool includes molecules that require ectoenzyme hydrolysis to be converted to labile matter. Bacteria utilization of the DOM is modeled by a hyperbolic function that is similar to Michaelis–Menton kinetics (Anderson and Williams, 1998; Anderson and Pondaven, 2003). Bacteria production and remineralization are modeled following Anderson and Williams (1998) and Walsh et al. (1999). Colored

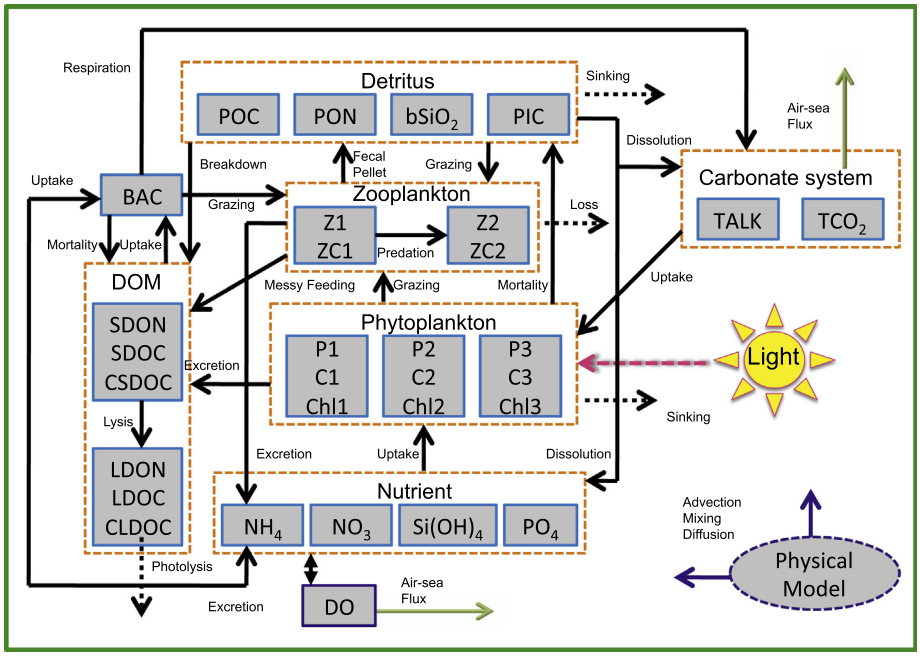

Fig. 1. The inter-compartmental flow chart of the biogeochemical model used in this study.

dissolved organic carbon (CDOC) modeled as a colored fraction of DOM through its production process is used to represent CDOM as in Bissett et al. (1999b). In the upper layer where light is strong, CDOC is destroyed via photolysis to produce DOC and TCO_2. In the deep ocean, the biogeochemical control on CDOC primarily arises from bacterial consumption and remineralization of sinking particles. Recent studies have also suggested the important role of ocean circulation and mixing in regulating CDOC abundance in deep waters, as observed apparent oxygen utilization (AOU) appears to explain a significant part of the CDOC variance (Swan et al., 2009; Yamashita and Tanoue, 2009; Nelson and Siegel, 2013).

2.2. Optical processes

Spectrally-resolved inherent optical properties (400–700 nm) including absorption and backscattering are explicitly represented in the model. The total absorption coefficient, $a(\lambda)$, is calculated from the sum of the absorption coefficients of seawater, phytoplankton, non-algal particles, and CDOM,

$$a(\lambda) = a_w(\lambda) + a_\varphi(\lambda) + a_{\mathrm{NAP}}(\lambda) + a_{\mathrm{CDOM}}(\lambda), \quad (1)$$

where $a_w(\lambda)$ is the absorption coefficient from seawater that can be obtained from Pope and Fry (1997).

Considering the phytoplankton photo-adaptive state, the chlorophyll-specific absorption coefficients, $a^*_{\varphi 1}(\lambda)$ and $a^*_{\varphi 2}(\lambda)$ for picoplankton and diatoms, are calculated as:

$$a^*_{\varphi 1}(\lambda) = a^*_{\varphi 1(high)}(\lambda) \times \left(1 - \frac{\frac{\mathrm{Chl1}}{\mathrm{C1}} - \theta^C_{\min}}{\theta^C_{\max} - \theta^C_{\min}}\right) + a^*_{\varphi 1(low)}(\lambda) \times \frac{\frac{\mathrm{Chl1}}{\mathrm{C1}} - \theta^C_{\min}}{\theta^C_{\max} - \theta^C_{\min}}, \quad (2)$$

$$a^*_{\varphi 2}(\lambda) = a^*_{\varphi 2(high)}(\lambda) \times \left(1 - \frac{\frac{\mathrm{Chl2}}{\mathrm{C2}} - \theta^C_{\min}}{\theta^C_{\max} - \theta^C_{\min}}\right) + a^*_{\varphi 2(low)}(\lambda) \times \frac{\frac{\mathrm{Chl2}}{\mathrm{C2}} - \theta^C_{\min}}{\theta^C_{\max} - \theta^C_{\min}}, \quad (3)$$

where $a^*_{\varphi 1(high)}(\lambda)$, $a^*_{\varphi 1(low)}(\lambda)$, $a^*_{\varphi 2(high)}(\lambda)$, and $a^*_{\varphi 2(low)}(\lambda)$ are chlorophyll-specific absorption coefficients for picoplankton and diatoms at high- and low-light levels (Fig. 2). According to Fujii et al. (2007), we set $\theta^C_{\min}$ and $\theta^C_{\max}$, the minimum and maximum chlorophyll to carbon ratios, to be 0.036 (mgChl mmolC^{-1}) and 1.2 (mgChl mmolC^{-1}), respectively. We do not consider the photo-adaptive state for coccolithophorids (Nanninga and Tyrrell, 1996). Total phytoplankton absorption coefficient, $a_\varphi(\lambda)$, is then calculated as:

$$a_\varphi(\lambda) = a^*_{\varphi 1}(\lambda) \times \mathrm{Chl1} + a^*_{\varphi 2}(\lambda) \times \mathrm{Chl2} + a^*_{\varphi 3}(\lambda) \times \mathrm{Chl3}. \quad (4)$$

Non-algal particle absorption coefficient, $a_{\mathrm{NAP}}(\lambda)$ is calculated as:

$$a_{\mathrm{NAP}}(\lambda) = a^*_{\mathrm{NAP}}(440) \times (\mathrm{POC} + \mathrm{PIC}) \times \exp\{-0.012 \times (\lambda - 440)\}, \quad (5)$$

where $a^*_{\mathrm{NAP}}(440)$ is the specific absorption coefficient at 440 nm that is fixed to be 0.0012 m^2 mmolC^{-1} (Babin et al., 2003a,b; Fujii et al., 2007). This specific absorption coefficient and the spectral slope (0.012 nm^{-1}) are the averaged values derived from a variety of environmental conditions, including highly organic samples in the Baltic Sea and highly mineral-dominated samples in the North Sea and English Channel (Babin et al., 2003a).

CDOM absorption coefficient is calculated with a spectral dependence:

$$a_{\mathrm{CDOM}}(\lambda) = a_{\mathrm{CDOC}}(410) \times \exp\{-0.0145 \times (\lambda - 410)\}, \quad (6)$$

$$a_{\mathrm{CDOC}}(410) = a^*_{\mathrm{cdoc}} \times (\mathrm{CSDOC} + \mathrm{CLDOC}), \quad (7)$$

where a^*_{cdoc} is the CDOC specific absorption coefficient at the reference wavelength of 410 nm. The absorption curve is determined by an exponential function with a spectral slope of 0.0145 nm^{-1} (Fujii et al., 2007). Based on the specific absorption coefficients of humic and fulvic acids of 2.63 and 1.40 m^2 gC^{-1}, respectively, measured at 410 nm (Zepp and Schlotzhauer, 1981), semi-labile CDOC specific absorption coefficient at 410 nm was estimated to be 0.061 m^2 mmolC^{-1} by assuming that 30% of the humus is colored fraction, as well as 10% of humus is humic acid and 90% of humus is fulvic acid (Wetzel et al., 1995; Bissett et al., 1999a). This calculation with the assumption that all CDOC comes from humic and fulvic acids is in a reasonable range for terrestrial-origin CDOC and the deep-ocean CDOC that are largely composed of humic and fulvic acids (Carder et al., 1989). In the upper layer of the open ocean, the CDOC

Table 1
Model parameters and their values.

Parameters	Symbol	Chai et al. (2002)	Fujii and Chai (2007)	Fujii et al. (2007)	This study	Reference
For plankton and zooplankton						
NH_4 inhibition for P1	ψ_1	5.59	5.59	5.59	5.59	(1), (2), (10)
NH_4 inhibition for P2	ψ_2	5.59	5.59	5.59	1.5	(1), (6)
NH_4 inhibition for P3	ψ_3	N/A	5.59	N/A	5.59	(1), (2), (10)
Half-saturation for NO_3 uptake by P1	K_{P1_NO3}	0.5	1.0	1.0	1.0	(2), (10)
Half-saturation for NH_4 uptake by P1	K_{P1_NH4}	0.05	0.1	0.05	0.1	(2)
Half-saturation for NO_3 uptake by P2	K_{P2_NO3}	N/A	N/A	N/A	3.0	(6)
Half-saturation for SiO_4 uptake by P2	K_{P2_SiO4}	3.0	3.0	3.0	4.5	(1), (6)
Half-saturation for NO_3 uptake by P3	K_{P3_NO3}	N/A	1.0	N/A	1.0	(2), (10)
Half-saturation for NH_4 uptake by P3	K_{P3_NH4}	N/A	1.0	N/A	1.0	(2)
P1 mortality	γ_3	N/A	N/A	N/A	0.02	(1), (6)
P2 mortality	γ_4	0.05	0.05	0.05	0.05	(1), (2), (10)
P3 mortality	γ_{10}	N/A	0.05	N/A	0.05	(2)
P1, P2, P3 exudation	ε_1, ε_2, ε_3	N/A	N/A	N/A	0.2,0.2,0.2	(4), (5), (6)
P1, P2, P3 excretion	ε_4, ε_5, ε_6	N/A	N/A	N/A	0.3,0.3,0.3	(4), (5), (6)
P2 sinking speed	W_1	1.0	1.0	1.0	1.0	(1), (2), (10)
P3 sinking speed	W_3	N/A	1.0	N/A	1.0	(2)
Z1 assimilation efficiency for N and C	γ_1	1.0	1.0	1.0	0.9	(1), (6)
Z2 assimilation efficiency for N	γ_2	0.75	0.75	0.75	0.7	(1), (6)
Z2 assimilation efficiency for C	γ_{22}	N/A	N/A	N/A	0.65	(5), (6)
Z1 messy feeding fraction	Φ_1	N/A	N/A	N/A	0.1	(4), (5), (6)
Z2 messy feeding fraction	Φ_2	N/A	N/A	N/A	0.2	(4), (5), (6)
Z1 excretion	reg_1	0.2	0.2	0.2	0.2	(1)
Z2 excretion	reg_2	0.1	0.1	0.1	0.1	(1)
Z2 loss rate	λ	0.05	0.05	0.05	0.05	(1)
Z1 maximum specific grazing rate	$G1_{max}$	1.35	1.25	1.35	1.55	(1), (6)
Z2 maximum specific grazing rate	$G2_{max}$	0.53	0.48	0.64	0.56	(1), (6)
Half-saturation for Z1 ingestion	$K1_{gr}$	0.5	0.5	0.5	0.5	(1)
Half-saturation for Z2 ingestion	$K2_{gr}$	0.25	0.25	0.25	0.25	(1)
Z1 grazing preference for P1	ρ_5	1.0	1.0	1.0	0.9	(1), (6)
Z1 grazing preference for BAC	ρ_6	N/A	N/A	N/A	0.1	(6)
Z2 grazing preference for P2	ρ_1	0.7	0.35	0.7	0.6	(1), (6)
Z2 grazing preference for Z1	ρ_2	0.2	0.2	0.2	0.2	(1)
Z2 grazing preference for PON	ρ_3	0.1	0.1	0.1	0.1	(1)
Z2 grazing preference for P3	ρ_4	N/A	0.35	N/A	0.1	(6)
Chlorophyll-specific initial slope of P vs. I curve for phytoplankton	α	N/A	N/A	0.25	0.25	(10)
Maximum P1 carbon-specific nitrogen-uptake rate	p^{C1}_{ref}	N/A	N/A	2.0	1.5	(10), (6)
Maximum P2 carbon-specific nitrogen-uptake rate	p^{C2}_{ref}	N/A	N/A	3.0	2.5	(10), (6)
Maximum P3 carbon-specific nitrogen-uptake rate	p^{C3}_{ref}	N/A	N/A	N/A	1.0	(2), (6)
Minimum phytoplankton N:C ratio	Q_{min}	N/A	N/A	0.034	0.06	(10), (6)
Maximum phytoplankton N:C ratio	Q_{max}	N/A	N/A	0.17	0.17	(10)
Maximum value of θ^N	θ^N_{max}	N/A	N/A	4.2	1.5	(10), (6)
Other parameters						
$bSiO_2$ sinking speed	W_4	20.0	20.0	20.0	20.0	(1)
PIC sinking speed	W_5	N/A	20.0	N/A	15.0	(2), (6)
PON sinking speed	W_6	10.0	10.0	10.0	10.0	(1), (9)
POC sinking speed	W_7	N/A	N/A	N/A	15.0	(6)
Labile fraction of produced DOM	β_1	N/A	N/A	N/A	0.8	(5), (6)
Labile fraction of phyto-excreted DOC	β_2	N/A	N/A	N/A	0.6	(5), (6)
Fraction uptake of LDOC by BAC	β_3	N/A	N/A	N/A	0.96	(6)
Nitrification rate	γ_7	N/A	0.025	0.0	0.05	(2), (6)
Cost of biosynthesis	ξ_{NO3}	N/A	N/A	2.33	2.33	(10)
Color fraction of LDOC	colorFR1	N/A	N/A	N/A	0.1	(11), (6)
Color fraction of SDOC	colorFR2	N/A	N/A	N/A	0.2	(11), (6)
PON dissolution rate	D_{PON}	N/A	0.01	0.0	0.01	(2), (8)
PIC dissolution rate	D_{PIC}	N/A	0.005	N/A	0.01	(2), (6)
DOM fraction P1, P2, P3 mortality	δ_1, δ_2, δ_3	N/A	N/A	N/A	0.5, 0.5, 0.5	(5), (6)
BAC C:N ratio	R_B	N/A	N/A	N/A	5.1	(5)
BAC mortality	γ_{12}	N/A	N/A	N/A	0.05	(3), (4), (6)
Phosphorus to nitrogen ratio	R_{PN}	N/A	N/A	N/A	0.0625	(6)
PIC to organic carbon ratio in P3	R_{CaC}	N/A	1.0	N/A	1.0	(2)
Maximum labile DOC or NH_4 uptake	μB_{max}	N/A	N/A	N/A	0.8	(7), (6)
Maximum SDOC hydrolysis	γ_{13}	N/A	N/A	N/A	0.7	(5), (6)
Half-saturation for NH_4 uptake	K_B	N/A	N/A	N/A	0.5	(5)
Half-saturation for LDOC uptake	K_L	N/A	N/A	N/A	25.0	(5)
Half-saturation for SDOC uptake	K_{SDOC}	N/A	N/A	N/A	417.0	(5)
Half-saturation for SDON uptake	K_{SDON}	N/A	N/A	N/A	35.3	(6)
Respired fraction of BAC growth	r_b	N/A	N/A	N/A	0.5	(7)
Oxygen to nitrate ratio	R_{O2No3}	N/A	N/A	N/A	8.625	(6)
Oxygen to ammonium ratio	R_{O2NH4}	N/A	N/A	N/A	6.625	(6)
Specific rate of conversion	RtUVLDOC	N/A	N/A	N/A	2.0	(11), (6)
Specific rate of conversion	RtUVSDOC	N/A	N/A	N/A	2.0	(11), (6)

(*continued on next page*)

Table 1 (*continued*)

Parameters	Symbol	Chai et al. (2002)	Fujii and Chai (2007)	Fujii et al. (2007)	This study	Reference
Specific rate of conversion	RtUVLDIC	N/A	N/A	N/A	4.0	(11), (6)
Specific rate of conversion	RtUVSDIC	N/A	N/A	N/A	4.0	(11), (6)

(1) Chai et al. (2002), Fujii and Chai (2007); (3) Tian et al. (2000); (4) Anderson and Williams (1998); (5) Anderson and Pondaven (2003); (6) this study; (7) Walsh et al. (1999); (8) Levy et al. (1998); (9) Kishi et al. (2007); (10) Fujii et al. (2007); (11) Bissett et al. (1999a).

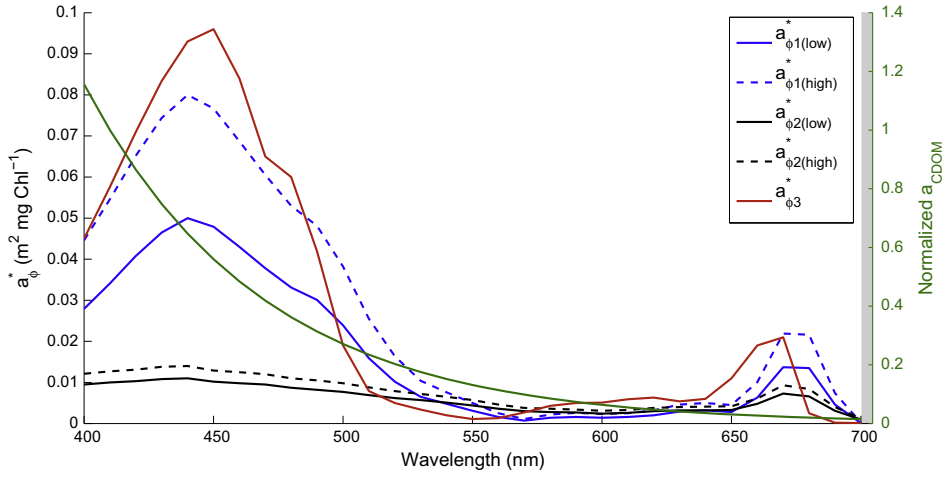

Fig. 2. Spectrally-resolved chlorophyll-specific absorption coefficients by picoplankton, diatoms, and coccolithophorids, and the CDOM absorption normalized at 410 nm. Both picoplankton and diatoms are modeled with photoadaption.

pool may also include amino acids and peptides, nucleic acids and bases, and other low-molecular-weight compounds. The specific absorption coefficients of these components are difficult to estimate as they are usually labile and susceptible to photolysis that may have gone through different light histories during different measurements. We thus use the same specific absorption coefficients for both labile and semi-labile CDOCs as suggested in Bissett et al. (2004). Our model sensitivity analysis has indicated that CDOC composition can affect upper ocean biogeochemical processes as it changes the ability of CDOC absorbing light. Assuming 100% of humic and 100% of fulvic acids in the CDOC composition result in the a^*_{cdoc} values of 0.1052 m^2 mmolC^{-1} and 0.056 m^2 mmolC^{-1}, which are about 72.5% higher and 8.2% lower than the value of 0.061 m^2 mmolC^{-1}, respectively. These differences can lead to primary production change as high as 20% in the euphotic zone. Due to the strong spatial variability, however, the magnitude of averaged primary production change over the North Pacific largely reduces to less than 5%.

Total backscattering coefficient, $b_b(\lambda)$, is calculated as the combined contribution from seawater and particles:

$$b_b(\lambda) = b_{bw}(\lambda) + b_{bp}(\lambda), \tag{8}$$

where $b_{bw}(\lambda)$ is the backscattering coefficient from seawater that can be obtained from Morel (1974).

Backscattering coefficient by total particles, $b_{bp}(\lambda)$, is expressed by:

$$b_{bp}(\lambda) = b_{bp1}(\lambda) + b_{bp2}(\lambda) + b_{bPIC}(\lambda) + bbg, \tag{9}$$

where $b_{bp1}(\lambda)$ and $b_{bp2}(\lambda)$ are the contributions from small and big sizes of the total particulate organic matter (TPOC), respectively. $b_{bPIC}(\lambda)$ is the backscattering coefficient from PIC, and *bbg* is the background backscattering that is fixed to 0.00017 (m^{-1}) (Fujii et al., 2007). Note that we use TPOC to represent the total organic carbon contained in any particles retained on a filter, including living biomass such as bacteria, algae and zooplankton, and non-living detritus such as decayed algae or fecal material, and that we use POC to represent detrital particulate organic carbon only. Based on Stramski et al. (1999), backscattering by small and large organic particles can be formulated as:

$$b_{bp1}(\lambda) = \left(\frac{\mathrm{TPOC1}}{476935.8}\right)^{1/1.277} \times \left(\frac{\lambda}{510}\right)^{-0.5}, \tag{10}$$

$$b_{bp2}(\lambda) = \left(\frac{\mathrm{TPOC2}}{17069.0}\right)^{1/0.859}, \tag{11}$$

where TPOC1 and TPOC2 are the small and big sizes of TPOC (unit: mgC m^{-3}), respectively. The spectral dependence is only set for small particles (Fujii et al., 2007), which are generally comprised of small phytoplankton, fine organic detritus, bacteria, and clay particles with a size of about 0.5–10 μm (Volkman and Tanoue, 2002). Seasonal field observations ranging from oligotrophic to eutrophic environments suggest there is a relatively consistent fraction of phytoplankton carbon to TPOC between 25% and 40% (Eppley et al., 1992; DuRand et al., 2001; Behrenfeld et al., 2005). By fixing this value to 30%, TPOC1 and TPOC2 are calculated from small phytoplankton carbon (picoplankton) and large phytoplankton carbon

(diatoms and coccolithophorids), respectively. The spectral variation of backscattering from PIC is estimated as in Gordon et al. (2001):

$$b_{bPIC}(\lambda) = b_{bPIC}(546) \times \left(\frac{\lambda}{546}\right)^{-1.35}, \quad (12)$$

where $b_{bPIC}(546)$ is the backscattering at 546 nm from PIC, which can be related to PIC concentration (Balch et al., 1996) by:

$$b_{bPIC}(546) = 0.0016 \times \mathrm{PIC} - 0.0036. \quad (13)$$

2.3. Light attenuation

With the spectrally-resolved optical properties, the underwater distribution of PAR is modeled as a function of water's absorption and backscattering coefficients. Based on numerical model simulations with different combinations of various levels of chlorophyll, CDOM, particles, and sun angles, Lee et al. (2005) developed a simple model for the vertical transmittance of visible light using absorption and backscattering coefficients at 490 nm, which uses a few empirical parameters and provides robust results for the underwater light field (Shulman et al., 2013). We use this method as our light attenuation scheme:

$$\mathrm{PAR}(z) = \mathrm{PAR}(0) \times e^{-K_{\mathrm{PAR}}(z)z}, \quad (14)$$

$$K_{\mathrm{PAR}}(z) = K_1 + \frac{K_2}{(1+z)^{0.5}}, \quad (15)$$

$$K_1 = [\chi_0 + \chi_1(a(490))^{0.5} + \chi_2 b_b(490)](1 + \alpha_0 \sin(\theta_a)), \quad (16)$$

$$K_2 = [\zeta_0 + \zeta_1 a(490) + \zeta_2 b_b(490)](\alpha_1 + \alpha_2 \cos(\theta_a)), \quad (17)$$

where θ_a is the solar zenith angle above the surface. K_1 and K_2 are model parameters with K_1 for asymptotic value at greater depth and K_2 more important for the subsurface light attenuation. PAR(0) is the PAR value at the sea surface. $\chi_{0,1,2}$, $\zeta_{0,1,2}$ and $\alpha_{0,1,2}$ are coefficients that can be obtained from Lee et al. (2005).

2.4. Physical model

The physical circulation model used in this study is based on the Regional Ocean Model System (ROMS), which represents an evolution in the family of terrain-following vertical coordinate models (Shchepetkin and McWilliams, 2005). ROMS solves the hydrostatic, primitive equations in the horizontal curvilinear coordinates. The model is configured for the Pacific Ocean (45°S to 65°N, 100°E to 70°W) at 50-km resolution, with realistic geometry and topography. There are 20 levels in the vertical. Near the two northern and southern walls, a sponge layer with a width of 5° from each wall is applied for temperature, salinity, and nutrients. In this study, the model is integrated during the period of 1980–2009, and we only analyze those outputs for the North and equatorial Pacific domain (20°S to 65°N, 100°E to 70°W).

Model temperature, salinity, nutrients (nitrate, silicate, and phosphate), and dissolved oxygen are initialized using data from the World Ocean Atlas 2005 (WOA05; Locarnini et al., 2006; Garcia et al., 2006). The initial conditions for TALK and TCO_2 are prescribed from the GLODAP dataset (Key et al., 2004). SDOC is set to 15 mmol m^{-3} at surface, decreases according to a hyperbolic tangent function to 0.01 mmol m^{-3} at 500 m, and is kept constant from there to the bottom. LDOC is set to 2.0 and 0.01 mmol m^{-3} between 0–500 m and between 500 m and the bottom, respectively. We use constant C:N ratios of 9.95 and 15.38 to initialize LDON and SDON, respectively. CLDOC and CSDOC are set to 0.01 mmol m^{-3} and 0.4 mmol m^{-3} over the water column, respectively. This leads to a CDOM absorption coefficient of ~0.15 m^{-1} at 320 nm in deep oceans, which is in the range of observations from the North Pacific (Swan et al., 2009; Yamashita and Tanoue, 2009). After the model calculation, constant background values representing refractory pools of 40 mmol m^{-3} and 2.6 mmol m^{-3} are added to represent the total DOC and DON products, respectively. BAC is initialized with 0.03 mmol m^{-3} at surface, decreases according to a hyperbolic tangent function to 0.01 mmol m^{-3} at 500 m, and is kept constant from there to the bottom. The initial conditions for other ecosystem variables are all set to 0.01 mmol m^{-3} for the model to spin up.

The model has been forced with the climatological air–sea fluxes of momentum, heat, and fresh water as well as preindustrial atmospheric CO_2 for 100 years to reach a quasi-equilibrium state. From this state, the model is integrated over the period of 1980–2009, forced with daily air–sea fluxes of momentum, heat, and fresh water derived from the National Centers for Environmental Prediction/National Center for Atmospheric Research (NCEP/NCAR) reanalysis (Kalnay et al., 1996). The surface wind stress is calculated from the 10-m wind based on the Large and Pond (1982) drag coefficient formulation. The heat flux is calculated from the prescribed shortwave and longwave radiations, and the sensible- and latent-heat fluxes that are calculated by the bulk formula with prescribed air temperature and relative humidity. The freshwater flux is derived from the prescribed precipitation from atmosphere, and evaporation is derived from the calculated latent-heat release.

2.5. Experimental design

In order to examine the impact of incorporating the optical processes in the model, we compare the control run (Control) with two test cases, Case1 and Case2. The control run is the one based on aforementioned parameterizations. In Case1, light attenuation is calculated based on phytoplankton biomass, which is routinely used by most ecosystem models (e.g., Chai et al., 2002; Fennel et al., 2003):

$$\mathrm{PAR}(z) = \mathrm{PAR}(0) \times \exp\left\{-k_1 z - k_2 \int_{-z}^{0} (\mathrm{P1} + \mathrm{P2} + \mathrm{P3}) dz\right\}, \quad (18)$$

where k_1 is the light attenuation due to seawater (0.046 m^{-1}), and k_2 is the light attenuation due to phytoplankton (0.03 m^{-1}). To study the contribution of CDOM, Case2 is designed with the same light attenuation scheme as the control run, but with a zero-CDOM absorption coefficient. The difference between Control and Case1 is different light attenuation calculations. The difference between Control and Case2 is CDOM attenuating light that is not accounted for in Case2. These two cases are conducted only during 1992–2009 using the control run result at the end of 1991 as the initial condition; the forcing and other parameters remain the same. To avoid model spin-up, we use the last 10-year outputs (2000–2009) from the case studies for analysis.

2.6. Data

Surface chlorophyll and carbon datasets from the Sea-viewing Wide Field-of-view Sensor (SeaWiFS) during September 1997 and December 2007 are used to evaluate model performance. The SeaWiFS carbon data is calculated from satellite-sensed particulate backscattering coefficient through empirical and regionally observed relationships (Behrenfeld et al., 2005). Primary production data derived by the SeaWiFS Vertically Generalized Production Model (VGPM; Behrenfeld and Falkowski, 1997) is used to compare modeled primary production.

Measured annual-mean climatological fields of nitrate (NO_3), silicate (SiO_4), and temperature are obtained from the WOA05.

In-situ measured nutrients and primary production from the Hawaii Ocean Time-series (HOT), and the California Cooperative Oceanic Fisheries Investigations (CalCOFI) are used to validate the model in these two regions. Two optical datasets are adopted to compare modeled optical properties, i.e., a_{φ}(440 or 443), a_{CDOM}(410 or 412), and b_{bp}(555). The first one is the Quasi-Analytical Algorithm (QAA) product derived from the SeaWiFS data (Lee et al., 2002). The second one is the in situ data measured in the CalCOFI region from the SeaWiFS BIO-optical Archive and Storage System (SeaBASS; Werdell and Bailey, 2002).

2.7. Statistics of model-observation fit

During the model evaluation against in situ or satellite observations, four kinds of statistics are used to quantify model-observation fit: model bias (Bias), root-mean-square error (RMSE), correlation coefficient (R), and standard deviation ratio (STDR). The bias (M-O) measures the mean deviation of the model (M) from the observation (O). A positive or negative bias reflects an overall overestimation or underestimation of the observations by the model, respectively. RMSE measures the deviation of the model from the observations in a squared sense. Correlation coefficient (R) measures the fit of the variations between model and observations. STDR gives the ratio of two standard deviations (M over O).

3. Results

3.1. Comparison of model outputs with data

To evaluate the ability of the model in reproducing dominant spatial and temporal patterns, modeled outputs are compared with observations based on monthly averages. Modeled climatological mean of depth-integrated (0–125 m) primary production (PP) shows a similar spatial pattern with SeaWiFS-derived VGPM, depicting high productivities (>700 mgC $m^{-2}d^{-1}$) in the eastern equatorial Pacific and northwest Pacific, as well as low productivities (<400 mgC m^{-2} d^{-1}) in the western equatorial and subtropical Pacific (Fig. 3). Due to the low spatial resolution, the model is unable to fully resolve coastal processes, and therefore misses those extremely high productivities (>1600 mgC m^{-2} d^{-1}) in the coastal regions. On the other hand, SeaWiFS-derived chlorophyll and subsequent primary production close to the continental margin might not be truly reliable owing to the strong interferences from suspended sediments, CDOM, and reflections from the ocean bottom (IOCCG, 2000). Away from the coastal region, the model tends to overestimate productions in the eastern and central equatorial Pacific. This discrepancy is expected because this region has been characterized as the high-nutrient-low-chlorophyll (HNLC) region limited by low supplies of iron (Martin et al., 1994; Coale et al., 1996). Without iron limitation on phytoplankton growth rates, the model is not able to accurately reproduce the biological activities there. Over the entire domain, there is a moderate correlation ($R = 0.57$) between model and VGPM, and the model shows a relatively lower standard deviation compared with the VGPM (STDR = 0.86).

Two boxes, representing Hawaii (HW) and California coastal (CF) regions, are chosen to compute area-averaged PP from the model for comparison with field measurements (Fig. 3). In-situ measured PP in HW is consistently higher than both the modeled and satellite PP (Fig. 4). The underestimation by the model could be related to the lack of nitrogen fixation in the biogeochemical model. Nitrogen fixation has been commonly observed to induce summer blooms in the subtropical gyre, where surface nitrate level is substantially low due to the strong stratification (Dore et al., 2008). The underestimation by the satellite is probably attributable to the unconstrained VGPM algorithm used to calculate PP in this region. Interestingly, the correlation between in situ and modeled PP is much higher than that between in situ and VGPM (0.53 vs. 0.15). The model depicts a similar seasonal pattern as the in situ PP, while the satellite VGPM seems to completely miss it. In-situ measured PP in the CF shows a strong seasonal pattern with highs around summer and lows in winter. Both the model and satellite can generally reproduce this pattern with comparable correlations to in situ PP (0.47 vs. 0.54), while the satellite VGPM tends to overestimate the seasonal peaks and winter magnitudes during each year. In-situ PP that is prone to be affected by small-scale features both in space and time, however, shows some anomalously high productions (>1000 mgC m^{-2} d^{-1}) that are not captured by either the satellite or the model that is not eddy resolving.

The model outputs optical properties with 10-nm interval in wavelength. We thus compare modeled a_{φ}(440), a_{CDOM}(410), and b_{bp}(550) with QAA-derived a_{φ}(443), a_{CDOM}(412), and b_{bp}(555), respectively. Modeled annual-mean a_{φ} shows large magnitudes in the eastern and central equatorial Pacific and North Pacific, as well as small magnitudes in the western equatorial and subtropical Pacific, in accordance with the satellite data with a robust correlation (Fig. 5 and Table 2). The model simulates lower spatial variability relative to the satellite data, which is likely related to the model's limited capability in modeling coastal processes or the satellite's overestimation in the coastal region. CDOM absorption coefficient, a_{CDOM}, shows a similar spatial pattern to a_{φ}, with large magnitudes in the eastern and central equatorial Pacific and North Pacific, and small magnitudes in the western equatorial and subtropical Pacific. The correlation coefficient between model and satellite is 0.65, while the model shows a relatively lower standard deviation due to the underestimation of a_{CDOM} in the northern part of the Pacific. In this region, vertical advection and diffusion have been suggested as main mechanisms for the upper-layer nutrient flux (Sumata et al., 2010). Thus, in addition to the biological sources, it is likely vertical CDOM flux is also important in regulating surface a_{CDOM} variability, and our 20-layer model may not be adequate to realistically resolve this process. Another possible reason could be due to the fact that the prescribed model initial condition for CDOM, especially below the mixed layer, is not universally representative over the entire Pacific basin. This can be potentially improved as more and more in situ data for CDOM become available. Modeled particulate backscattering coefficient, b_{bp}, shows a similar spatial pattern to modeled a_{φ}, suggesting its biological origin, which is different from the satellite b_{bp}, especially in the equatorial Pacific where the high scattering tongue stretching from the east is much wider than that in the model. The discrepancy is probably caused by the particle aggregation or other particle sources that are not included in the biological model. The correlation between model and satellite is moderate, and the bias is considerably low, due to the overestimation in the North Pacific and underestimation in the subtropical gyre, which also increases the standard deviation compared with that from the satellite data.

Historical optical measurements from SeaBASS, nutrients data from CalCOFI and HOT are compiled together to compare with modeled variables in the CF and HW regions (Fig. 6). Modeled nitrate and silicate concentrations fall in the observed ranges, with low values at the surface and high values at depth. Modeled phytoplankton absorption shows a subsurface maximum around 50 m in both January and July, which is not clearly shown in the SeaBASS dataset that covers both coastal and open oceans but is consistent with the open-ocean observation in the California Current System (Millan-Nuñez et al., 1996). Due to strong light destruction, modeled CDOM absorption at the surface is considerably lower in July than in January. Together with enhanced subsurface phytoplankton production, it results in a shallower and stronger subsurface CDOM absorption maximum in July. This is

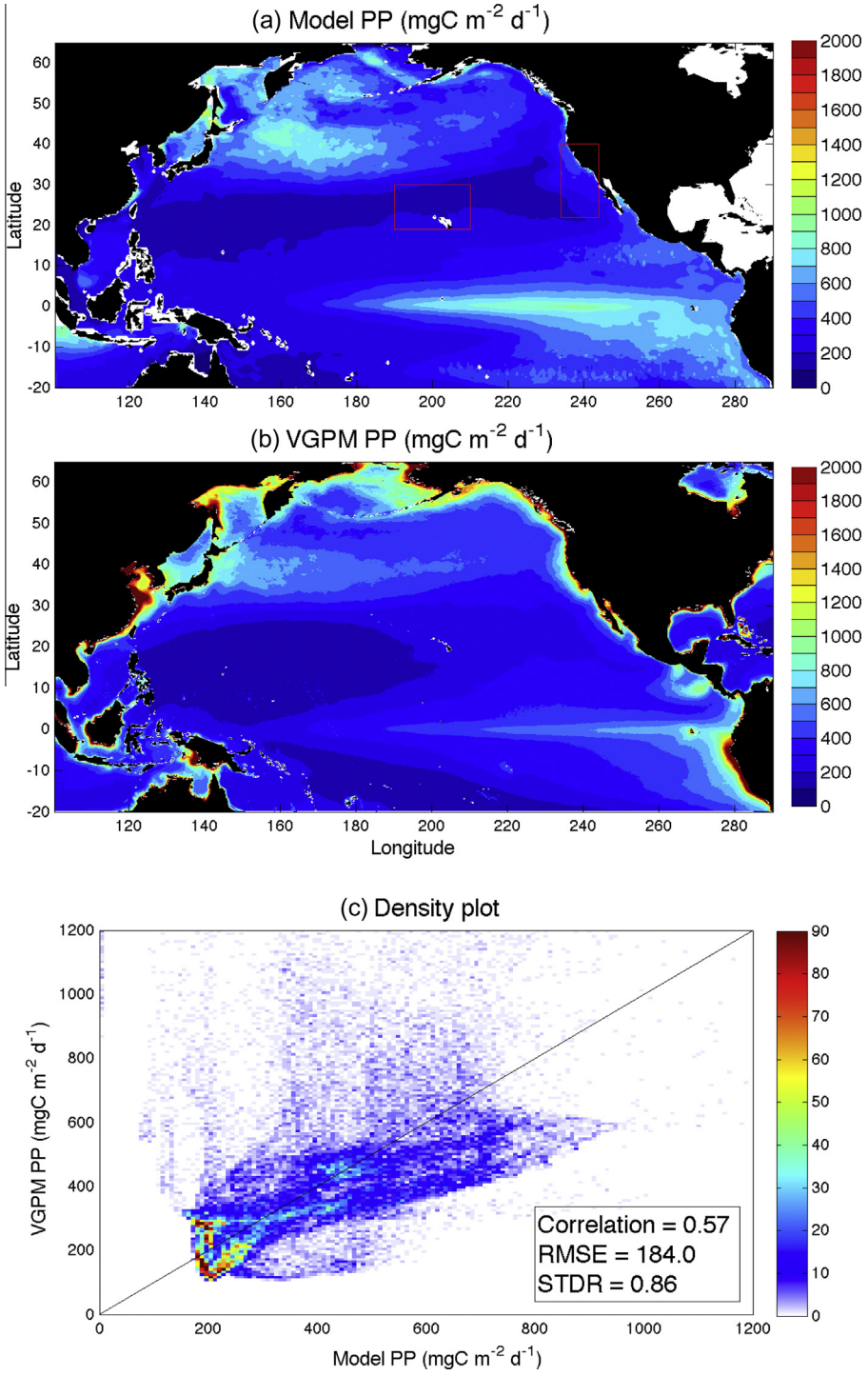

Fig. 3. Comparison of modeled depth-integrated primary production (0–125 m) (a) with SeaWiFS-derived VGPM primary production (b) averaged over 1997–2007. (c): Data density plot with red denoting high density and blue, low density. Two boxes in (a) mark the locations of Hawaii region (HW) and California region (CF). (For interpretation of the references to color in this figure legend, the reader is referred to the web version of this article.)

not clear from the in situ data, probably due to the influence of coastal CDOM sources (e.g., sediments, river runoffs). In the HW region, modeled nutrients can generally capture observed vertical distribution patterns (Fig. 6).

3.2. Optical and biological processes

Light distribution controlled by chlorophyll concentration in Case1 indicates higher values over the water column relative to the control run that is controlled by water optical properties (Fig. 7). It occurs along both zonal and meridional sections, where strong PAR differences between Control and Case1 are found in the upper 60 m and these differences could reach about 125 m, affecting the biological activity over the entire euphotic zone. Furthermore, the impact of CDOM contribution to light attenuation is mostly non-uniform at depth because of the non-uniform distribution of CDOM. Note that we use a zero CDOM absorption coefficient in Case2. This value can be increased to a constant value

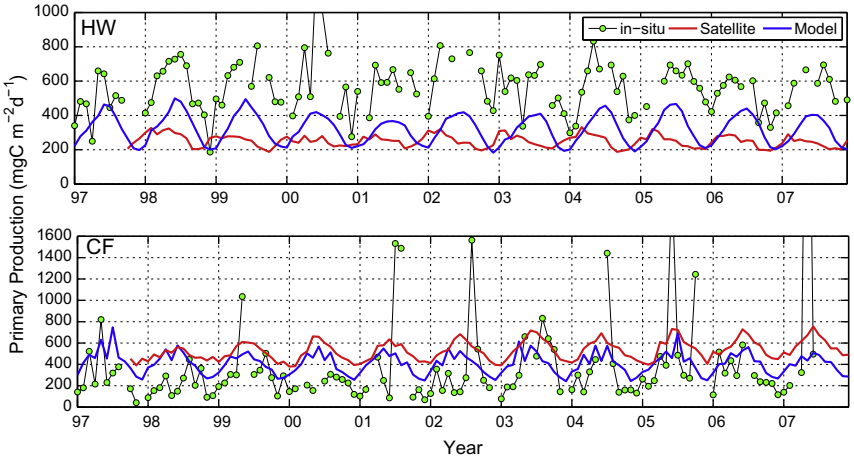

Fig. 4. Comparison of modeled depth-integrated PP with satellite VGPM product and in situ data in the HW and CF regions.

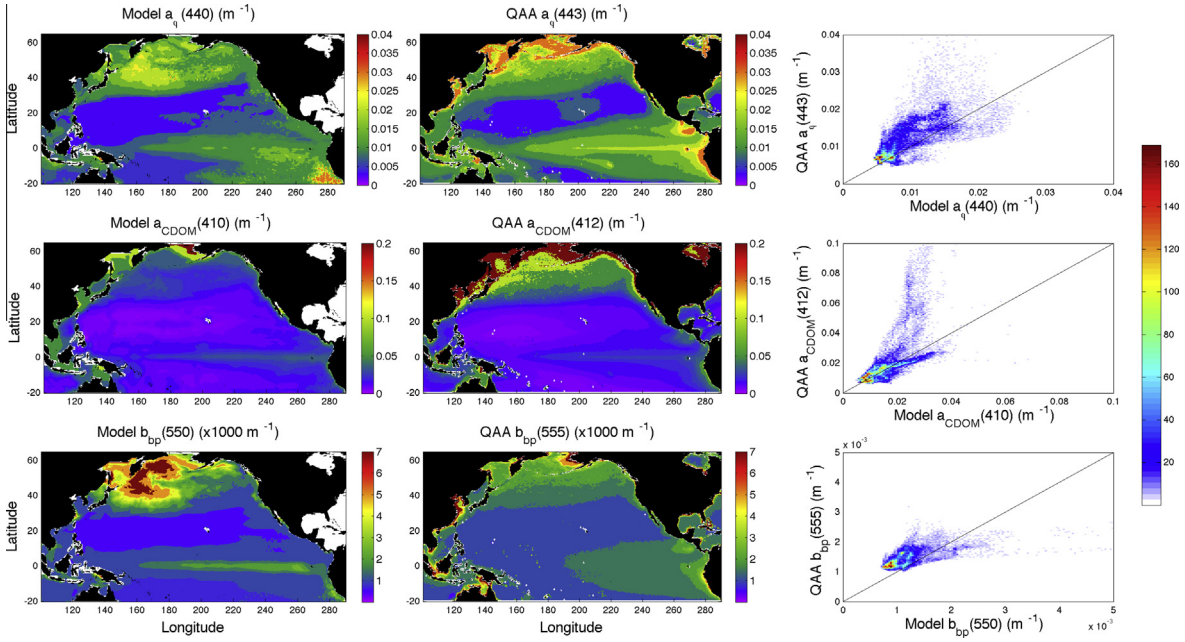

Fig. 5. Left panels: modeled $a_{\varphi}(440)$, $a_{CDOM}(410)$, and $b_{bp}(550)$ averaged over 1997–2007. Middle panels: SeaWiFS QAA derived $a_{\varphi}(443)$, $a_{CDOM}(412)$, and $b_{bp}(555)$ averaged over 1997–2007. Right panels: data density plot between model and QAA product with red denoting high density and blue, low density. (For interpretation of the references to color in this figure legend, the reader is referred to the web version of this article.)

Table 2
Statistical results between modeled $a_{\varphi}(440)$, $a_{CDOM}(410)$, $b_{bp}(550)$ and SeaWiFS QAA derived $a_{\varphi}(443)$, $a_{CDOM}(412)$, $b_{bp}(555)$ averaged over 1997–2007 (Fig. 5).

Model vs. QAA	a_{φ} (440,443)	a_{CDOM} (410,412)	b_{bp} (550,555)
R	0.62	0.65	0.53
RMSE (m^{-1})	0.0065	0.017	0.0011
STDR	0.69	0.54	1.7
Bias (m^{-1})	-3.1×10^{-3}	-6.3×10^{-3}	-2.7×10^{-5}

empirically as in Fujii et al. (2007), which will change the magnitude or the sign of the PAR difference between Case2 and Control but still will not generate the substantial spatial variability shown in Control. This is also true for Case1, because the tunable parameters (k_1 and k_2) in Eq. (18) are spatially constant. Therefore, the results shown here mainly illustrate the importance of including a detailed CDOM spatial structure to the underwater optical and biological fields.

After entering the water column, visible and shortwave lights are attenuated due to the absorption and scattering mostly by phytoplankton, CDOM, and non-algal particles. The remaining light at each depth will then serve as the source for phytoplankton's photosynthetic growth. Inaccurate light attenuation treatment in the model will likely lead to biased phytoplankton production and subsequent carbon export to the deep ocean. Compared with the empirical calculation in Case1, modeled phytoplankton chlorophyll concentration across 30°N shows a much shallower subsurface maximum and a relatively smaller magnitude in both western and eastern basins, suggesting more light entering deep water because of less attenuation in Case1 (Fig. 8). However, the modeled chlorophyll difference between Control and Case1 shows a non-uniform pattern (Fig. 9). There is little difference in the surface layer because of ample light for phytoplankton growth and low surface chlorophyll. In the subsurface layer around 40 m, even though light in Case1 is stronger than that in Control, modeled

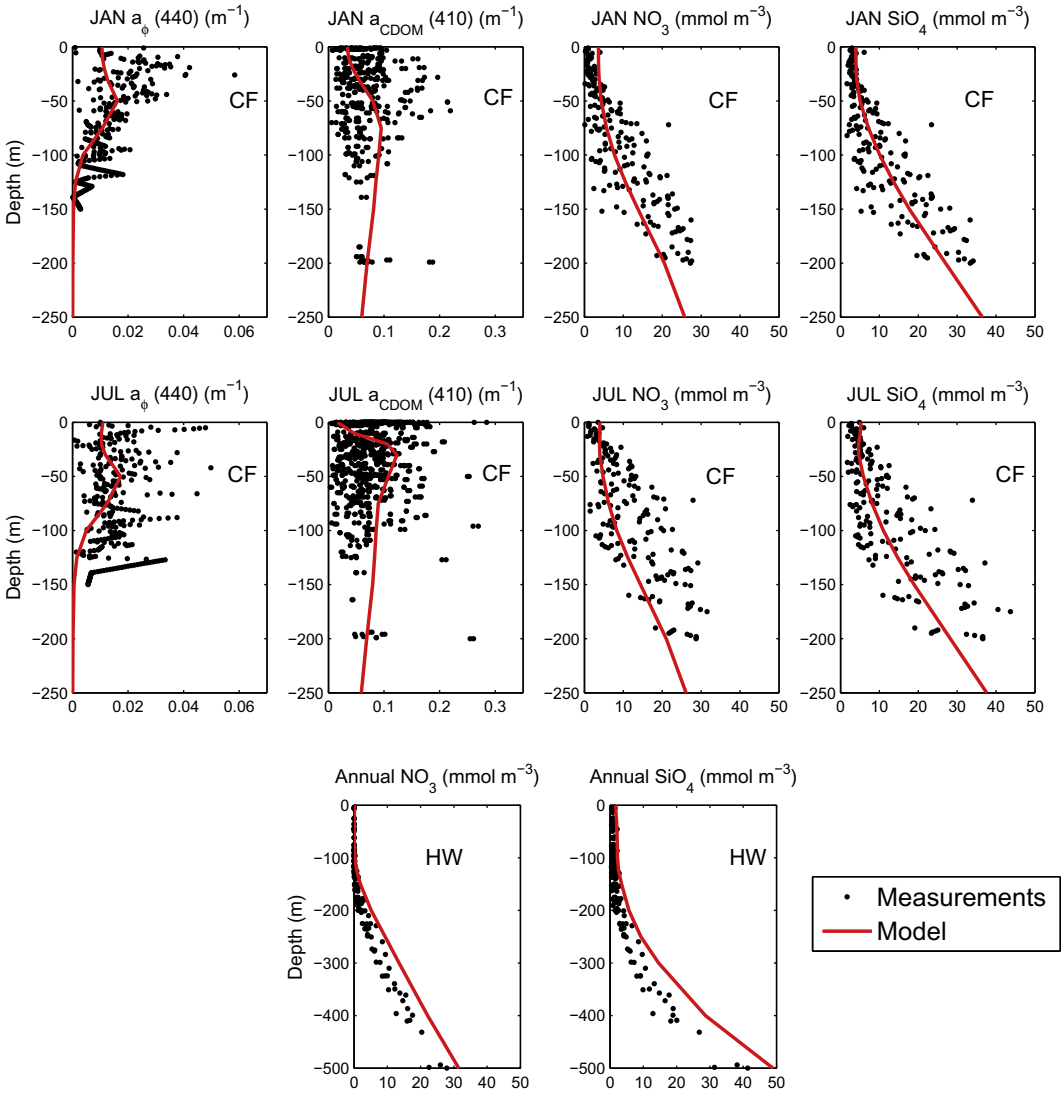

Fig. 6. Historical optical measurements from SeaBASS and nutrients data from CalCOFI are compiled together to compare with modeled variables averaged during the observation period in the CF region. Bottom panels show a comparison of modeled annual-mean nutrients with measurements in the HW region.

chlorophyll in Case1 is approximately 0.1–0.3 mg m^{-3} lower than that in Control. This is probably caused by the nutrient reduction due to the increased subsurface chlorophyll leading to reduced nutrient concentration in the upper layer. Phytoplankton's photoadaption to light levels could also result in decreased phytoplankton chlorophyll under enhanced light condition, especially when light is not a severely limiting factor for phytoplankton growth. In deep waters where light is a dominant factor for phytoplankton growth, stronger light in Case1 consequently leads to higher chlorophyll concentration, where the difference can reach 0.5 mg m^{-3} in this case. Another cross-section along 110°W shows similar features, in which deeper and stronger subsurface chlorophyll maximum is observed in Case1 relative to the control run (Fig. 8). As the chlorophyll in Control is high in both surface and subsurface at the equator, Case1 has lower chlorophyll concentration in the top 50 m and higher concentration below (Fig. 9). This is a little different from the subtropical gyre where the difference between Case1 and Control is relatively small in the top 20 m. Meridionally, chlorophyll difference shows an asymmetric vertical structure across the equator with shallow and strong subsurface maximum in the Northern Hemisphere, and deep and weak subsurface maximum in the Southern Hemisphere, which resembles the vertical chlorophyll pattern in Control (Fig. 9). Normally, tuning k_2 in Eq. (18) can generate a better underwater light field close to Control. By doing so, one assumes adding another light-attenuating constitute in the water column that co-varies with phytoplankton biomass. However, in most cases CDOM and particles do not co-vary with phytoplankton and tend to show strong spatial and temporal variability that is regulated not only by biological but also physical processes.

CDOM, often ignored in biological models, attenuates light mostly by absorption. To examine its influence on biological fields, CDOM absorption coefficient is set to zero in Case2 (Fig. 8). The resultant vertical chlorophyll in both cross-sections shows stronger and deeper subsurface maximum compared with that in the control run. Along 30°N, the chlorophyll difference between Case2 and Control is relatively small in the surface layer (Fig. 9). Case2 shows reduced chlorophyll concentration around 40 m in the west, and generally elevated values below 80 m across the basin. In the meridional cross-section, the asymmetric structure still exists. Compared with the control run, Case2 shows much lower chlorophyll concentrations between 30 and 60 m and higher values below 60 m in the Northern Hemisphere, while it only shows a conspicuous enhancement below 60 m in the Southern

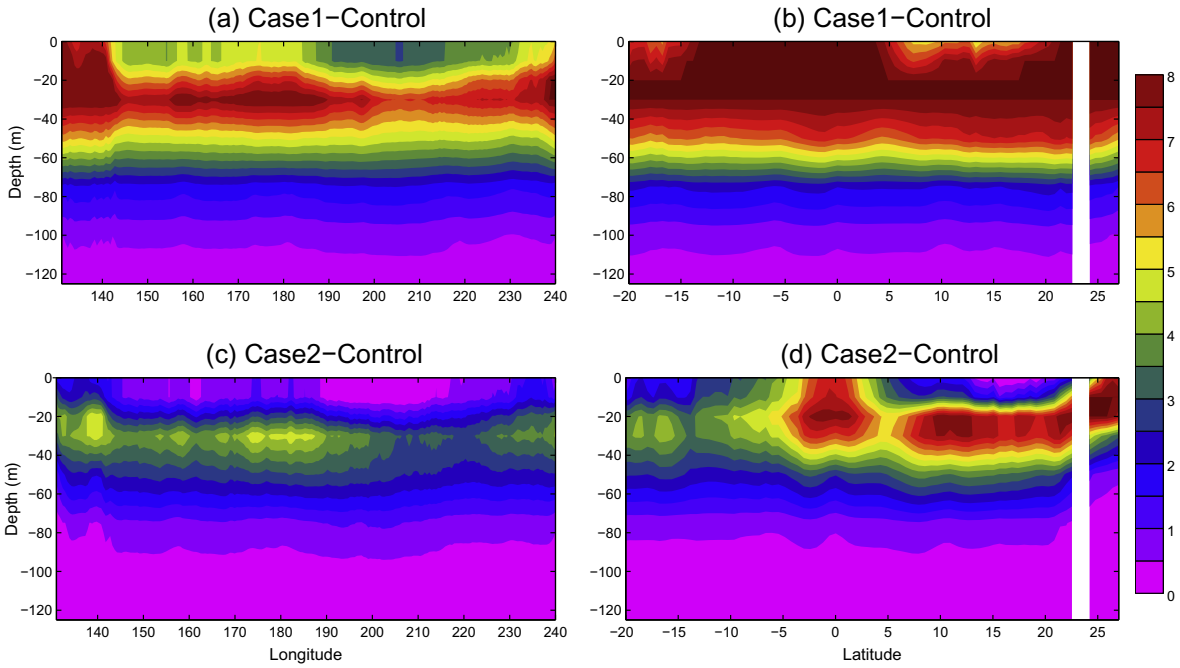

Fig. 7. Modeled PAR differences (w m^{-2}) between Control and Case1 (top), and between Control and Case2 (bottom), along 30°N (left panels) and 110°W (right panels).

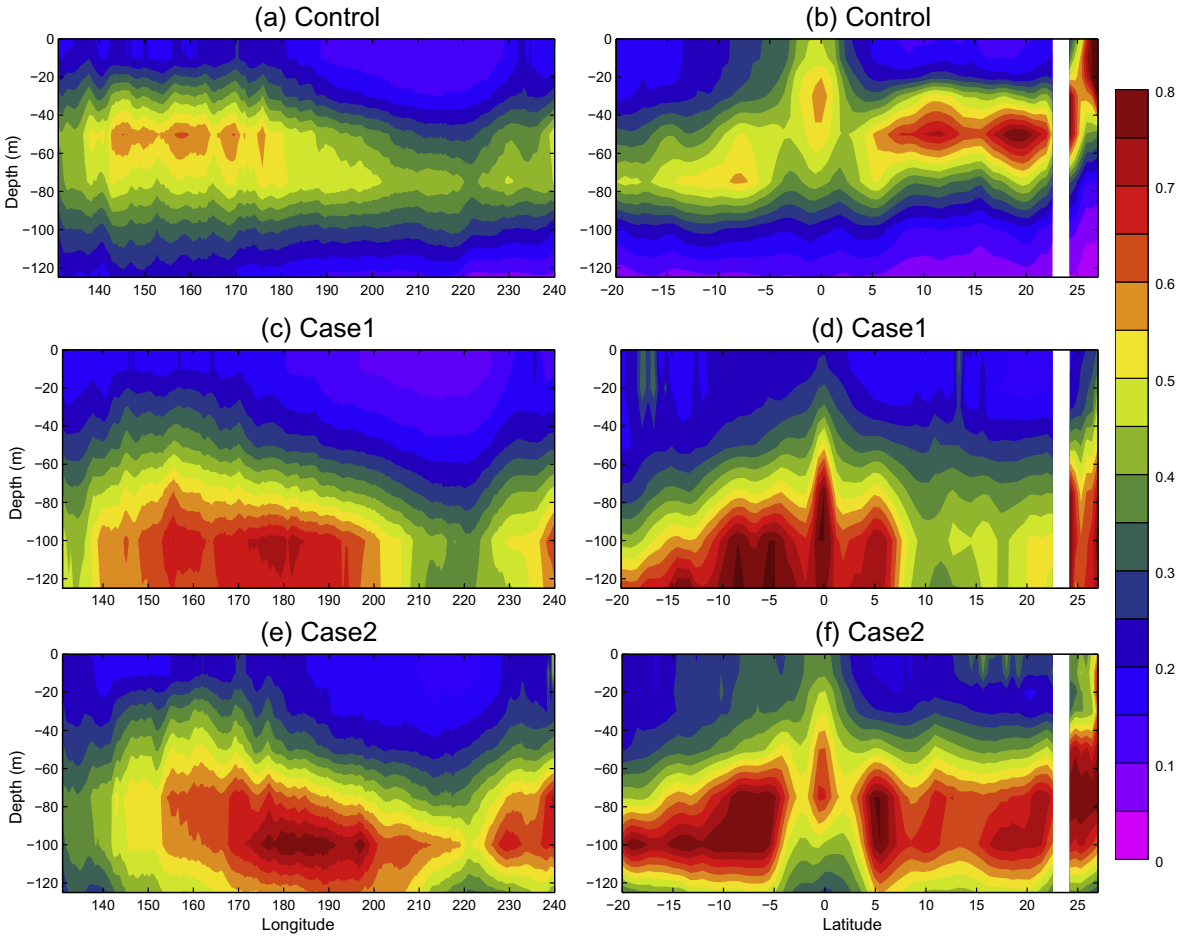

Fig. 8. Modeled mean chlorophyll concentration (mgChl m^{-3}) along 30°N (left panels) and 110°W (right panels) for Control (top), Case1 (middle), and Case2 (bottom).

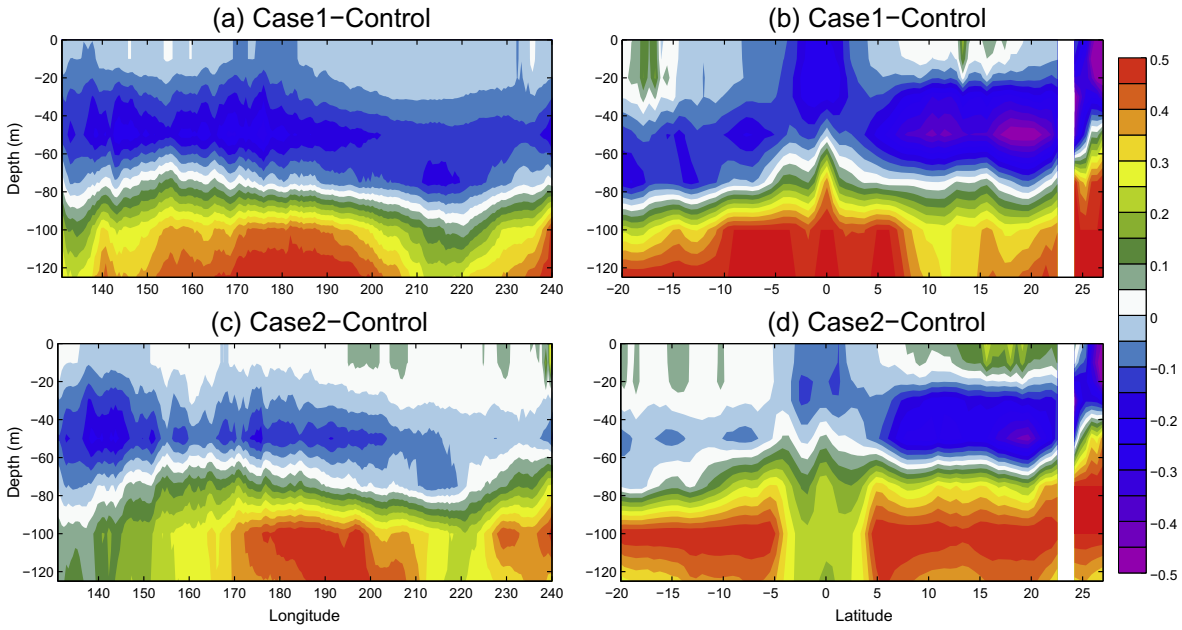

Fig. 9. Modeled chlorophyll concentration differences (mgChl m^{-3}) between Control and Case1 (top), and between Control and Case2 (bottom), along 30°N (left panels) and 110°W (right panels).

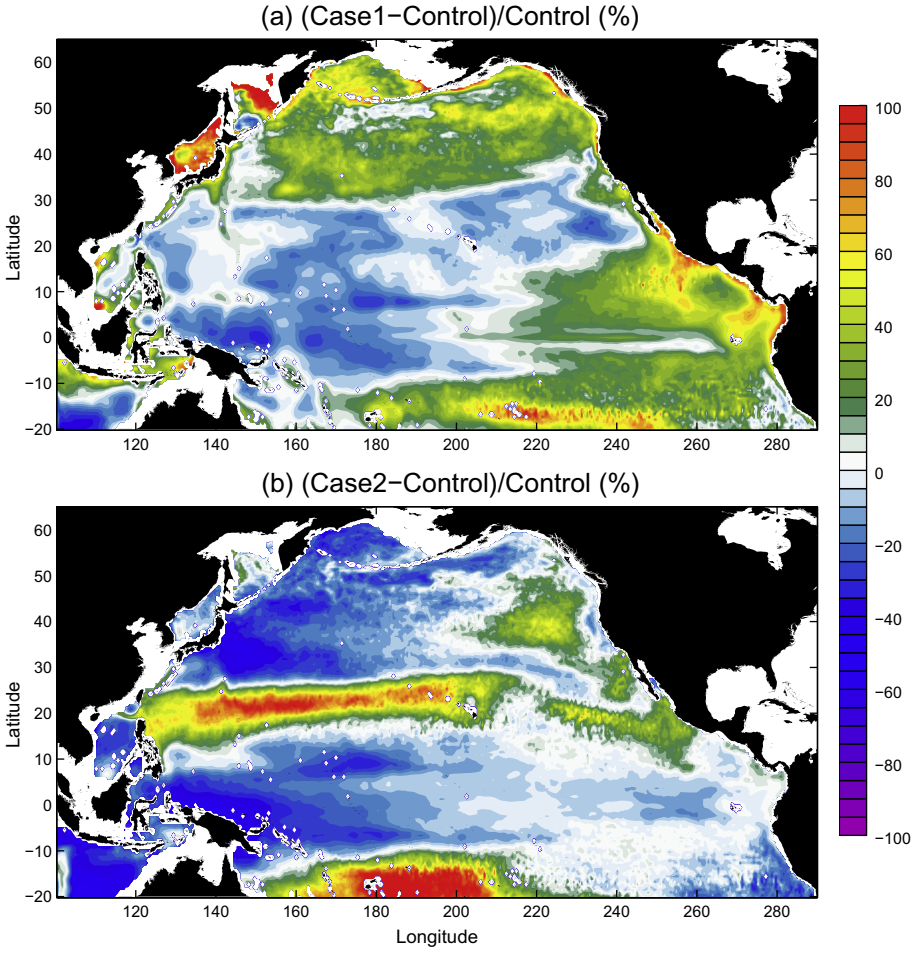

Fig. 10. Percentile differences of modeled depth-integrated PP averaged during 2000–2009 between Control and Case1 (a), and between Control and Case2 (b).

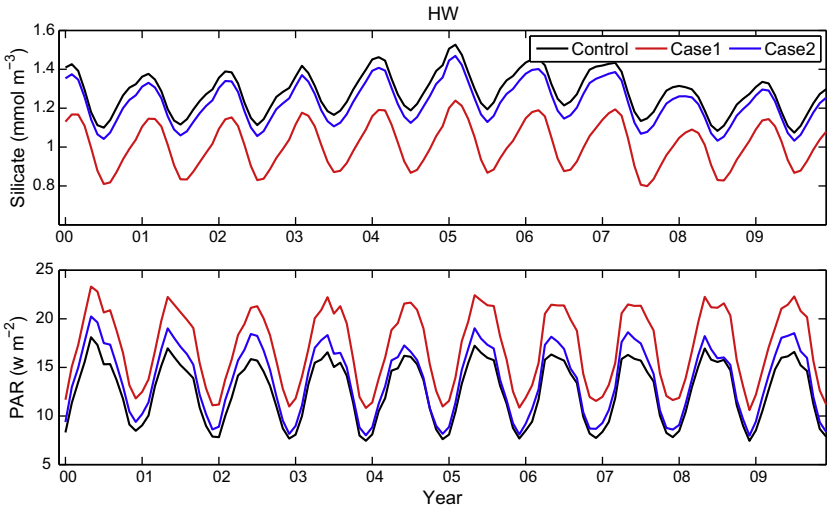

Fig. 11. Time series of depth-integrated mean of silicate concentrations and PAR values over the top 125 m in the HW region.

Hemisphere, which implies the importance of the spatial variability in CDOM distribution to underwater light field that controls biological production.

The spatial distribution of the depth-integrated PP difference between Control and Case1 indicates that the light treatment in Case1 could lead to primary production 50% higher in the eastern equatorial Pacific and North Pacific than in the control run (Fig. 10a). In the subtropical gyre, the PP difference is relatively small, about 10% lower in Case1. While in the western equatorial Pacific, Case1 appears to have about 25% lower PP than the control run. Over the entire basin, the mean PP difference between Case1 and Control is about 14%, comparable with the 10% between Case2 and Control. Without considering CDOM absorption in Case2, about 33% of the domain area is covered with less than 10% PP difference (Fig. 10b). Relative to Control, higher values of PP (relative difference >10%) in Case2 possessing about 39% of the total domain area, occur in the eastern North Pacific, a latitudinal band between 15° and 25°N stretching from the Luzon Strait to the Hawaii Islands, as well as a patch between 160° and 210°E in the Southern-Hemisphere subtropical gyre, with the largest difference reaching over 100%. In comparison, about 29% of the domain area is covered with significantly lower PP in Case2 compared with Control (relative difference <−10%), and most of it is located in the western basin.

PP differences generated in the two cases could be related to both nutrients and light differences. Because of different light attenuation schemes used in Case1 and Control, averaged light level in the euphotic zone is higher in the subtropical gyre in Case1 than in Control (Fig. 11). As shown here, this elevated light level leads to enhanced phytoplankton biomass in the lower euphotic zone, which further drives nutrients level down. Given that the general source for surface nutrients is from subsurface via vertical mixing or upwelling, reduced nutrient concentrations in the lower euphotic zone can also lead to reduced nutrient levels in the upper layer. Low PP in Case1 in this region is thus primarily attributed to the reduced nutrient concentrations instead of enhanced light levels. Without CDOM absorption, Case2 also produces higher light levels relative to the control run, especially during summer (Fig. 11). Similarly, lower nutrients are found in Case2 in the euphotic zone compared with those in the control run. The higher PP in Case2 is therefore more related to enhanced light levels. In other regions such as the northwest Pacific, CDOM-induced light difference cannot offset nutrient difference, leading to PP difference attributable to different nutrient conditions. This suggests that CDOM absorption as well as its spatial variability can regulate local biological productivity by changing both underwater light and nutrient conditions.

Different light treatments in the model generate different underwater light field that subsequent changes phytoplankton productivity. Changes in phytoplankton biomass, and corresponding CDOM and detritus concentrations, will then modify total absorption and backscattering coefficients in the water column that can further feedback to the underwater light field. With modified chlorophyll concentrations in Case1 and Case2, phytoplankton absorption differences between Control and Case1 and between Control and Case2 show similar patterns in response to the chlorophyll differences, where Case1 shows lower and higher absorption coefficients in the upper and lower layers, respectively, while Case2 generally shows lower values in the mid-layer between 20 and 60 m than those in the control run (Fig. 12).

3.3. CDOM analysis

As indicated in Fujii et al. (2007), their modeled biogeochemical properties are most sensitive to changes in CDOM absorption. Without CDOM in the biogeochemical model, light would be otherwise absorbed by phytoplankton alone. This impact can be more pronounced for picoplankton and coccolithophorids than for diatoms due to different absorbing capabilities in the blue wavelength where CDOM absorbs (Fig. 2), which results in changes in phytoplankton community structure and other biogeochemical properties. Modeled CDOM concentration has indicated substantial spatial variability across the Pacific basin (Fig. 13). Although resembling the spatial pattern of phytoplankton chlorophyll, modulations of CDOM in the upper ocean are subject to complex interactions of physical and biogeochemical processes. The dynamic detail of CDOM regulation mechanisms is therefore further analyzed through term-by-term diagnosis of its governing equation in the model:

$$\frac{\partial \mathrm{CDOM}}{\partial t} = -u\frac{\partial \mathrm{CDOM}}{\partial x} - v\frac{\partial \mathrm{CDOM}}{\partial y} - w\frac{\partial \mathrm{CDOM}}{\partial z} + \frac{\partial}{\partial z}\left(K_V \frac{\partial \mathrm{CDOM}}{\partial z}\right) + K_H \Delta_H \mathrm{CDOM} + \mathrm{BIO}. \quad (19)$$

To identify the key dynamic processes for CDOM, we examine the relative importance of these terms: local rate of change (LRC:

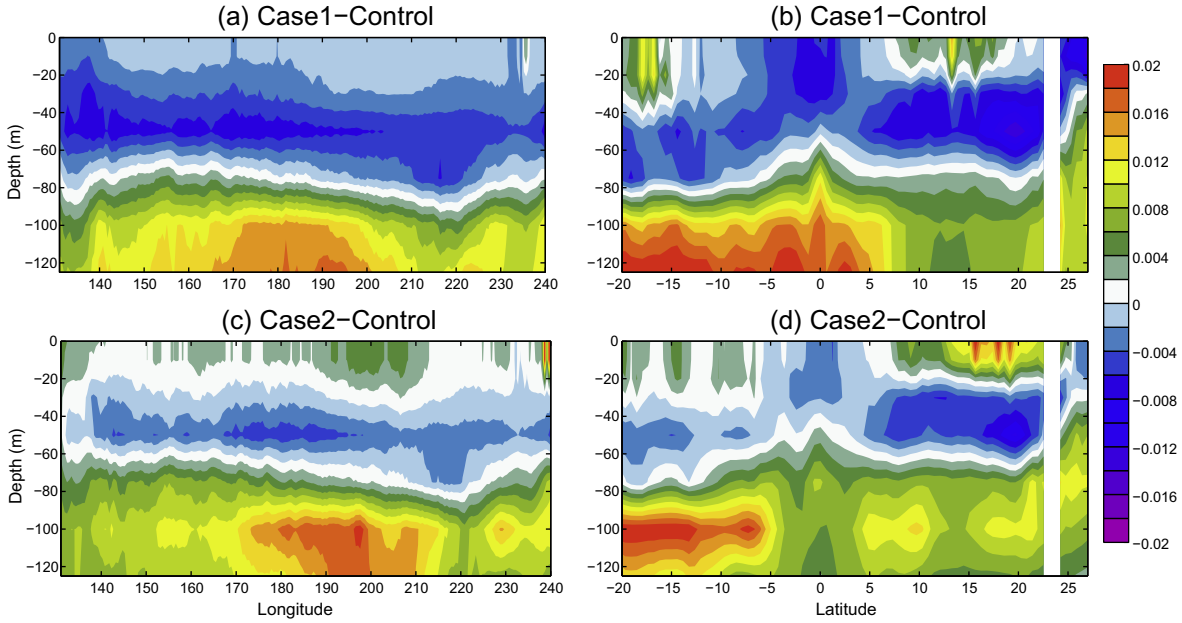

Fig. 12. Modeled phytoplankton absorption coefficient differences (m^{-1}) between Control and Case1 (top), and between Control and Case2 (bottom) along 30°N (left panels) and 110°W (right panels).

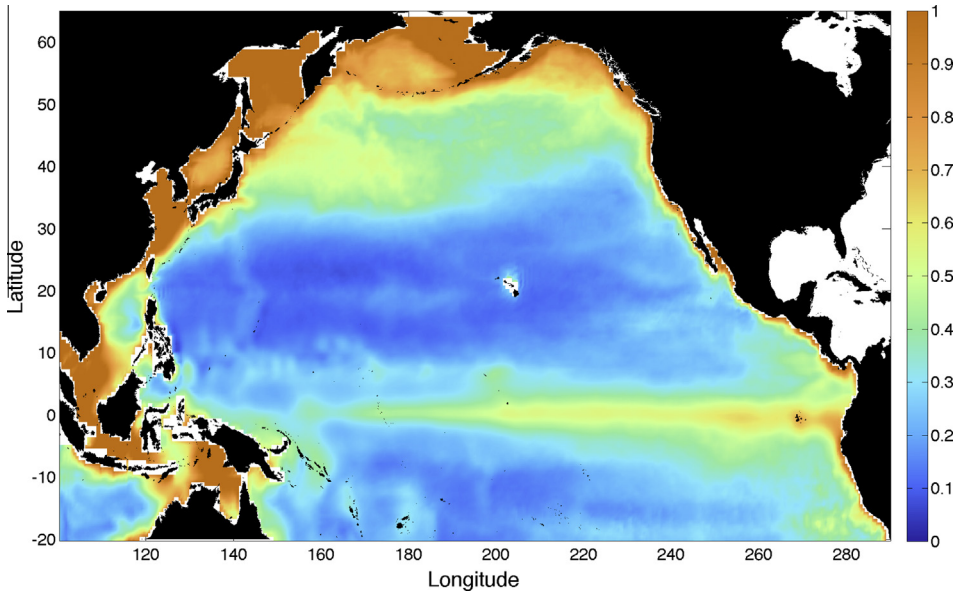

Fig. 13. Modeled sea surface CDOC concentrations (mmolC m^{-3}) averaged over 1997–2007.

$\frac{\partial CDOM}{\partial t}$), zonal advection (UADV: $-u\frac{\partial CDOM}{\partial x}$), meridional advection (VADV: $-v\frac{\partial CDOM}{\partial y}$), vertical advection (WADV: $-w\frac{\partial CDOM}{\partial z}$), vertical mixing (VMIX: $\frac{\partial}{\partial z}(K_V\frac{\partial CDOM}{\partial z})$), horizontal mixing (HMIX: $K_H\Delta_H$-CDOM), and the biological contribution (BIO).

To understand the CDOM dynamics in the entire euphotic zone, we integrate these terms from surface to 125-m depth. Two-year time series of these terms in the HW and CF regions are shown in Fig. 14. In these two regions, biological processes dominate the seasonal cycle of modeled LRC, which peaks in spring and reaches the minimum in winter. Mixing terms, including horizontal and vertical mixing, have much lower amplitudes that are about two orders of magnitude smaller than the BIO. The seasonal variability of horizontal and vertical advections is about one order of magnitude smaller than the BIO. Unlike BIO with seasonality changing sign over one year, however, horizontal advections (LADV = UADV + VADV) in these two regions are generally positive, and vertical advection (WADV) is negative during much of the year. Therefore, the annual-mean flux is different from the seasonal variability, where vertical advection is the dominant term that tends to reduce CDOM concentration in the euphotic zone in the HW region (Fig. 16). Both UADV and VADV are positive in the HW region, resulting in an increase of CDOM concentration. Mixing terms, including a positive HMIX and a negative VMIX, are still small compared to the other terms. The combined physical processes are approximately balanced by the positive BIO, leading to a relatively small annual LRC term in this region.

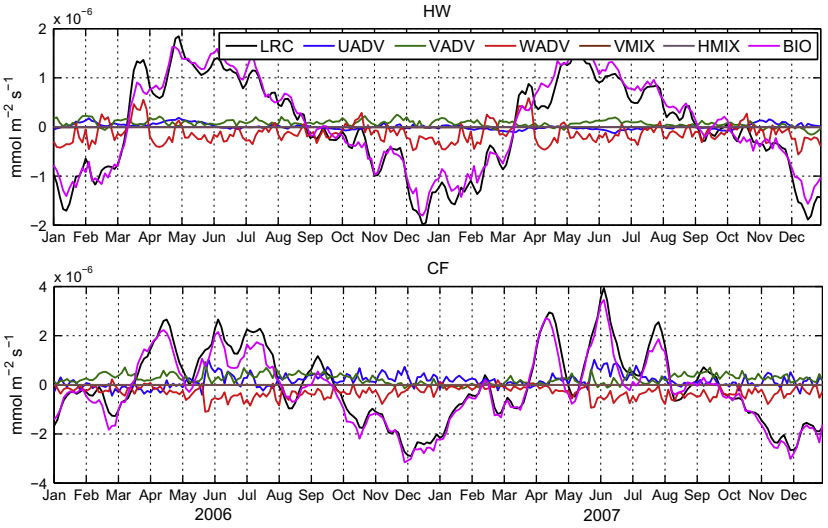

Fig. 14. Modeled CDOM regulation terms in the HW and CF regions for 2006 and 2007. The temporal resolution is three days. LRC: local rate of change, UADV: zonal advection, VADV: meridional advection, WADV: vertical advection, VMIX: vertical mixing, HMIX: horizontal mixing, and BIO: biological contribution.

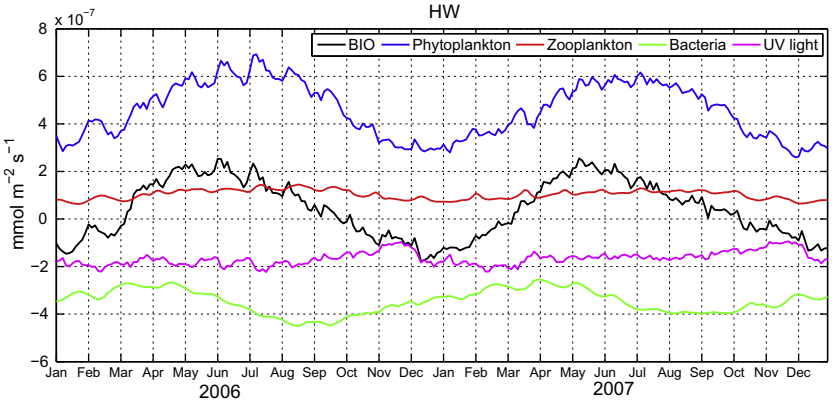

Fig. 15. Decomposition of the BIO term into contributions from phytoplankton, zooplankton, bacteria, and UV light in the HW region for 2006 and 2007.

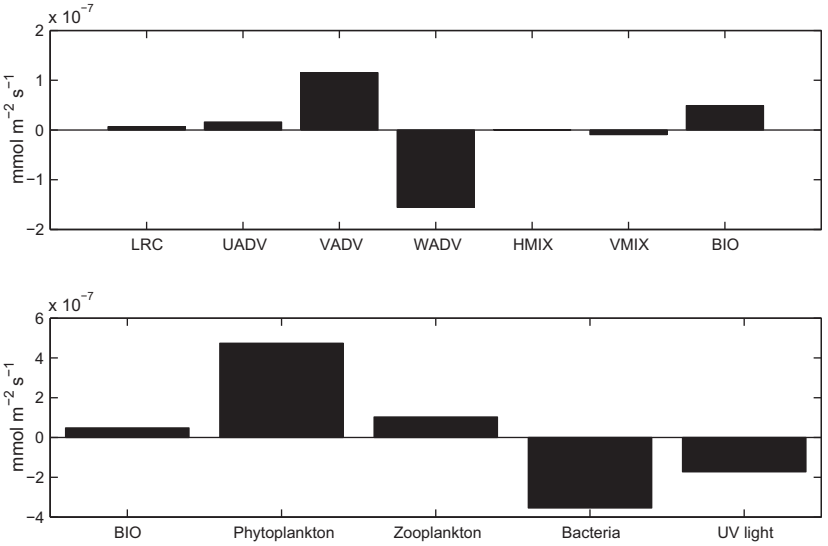

Fig. 16. Top: annual-mean regulation terms for CDOM in the HW region. Bottom: decomposition of the annual-mean BIO into contributions from phytoplankton, zooplankton, bacteria, and UV light calculated from the biogeochemical model.

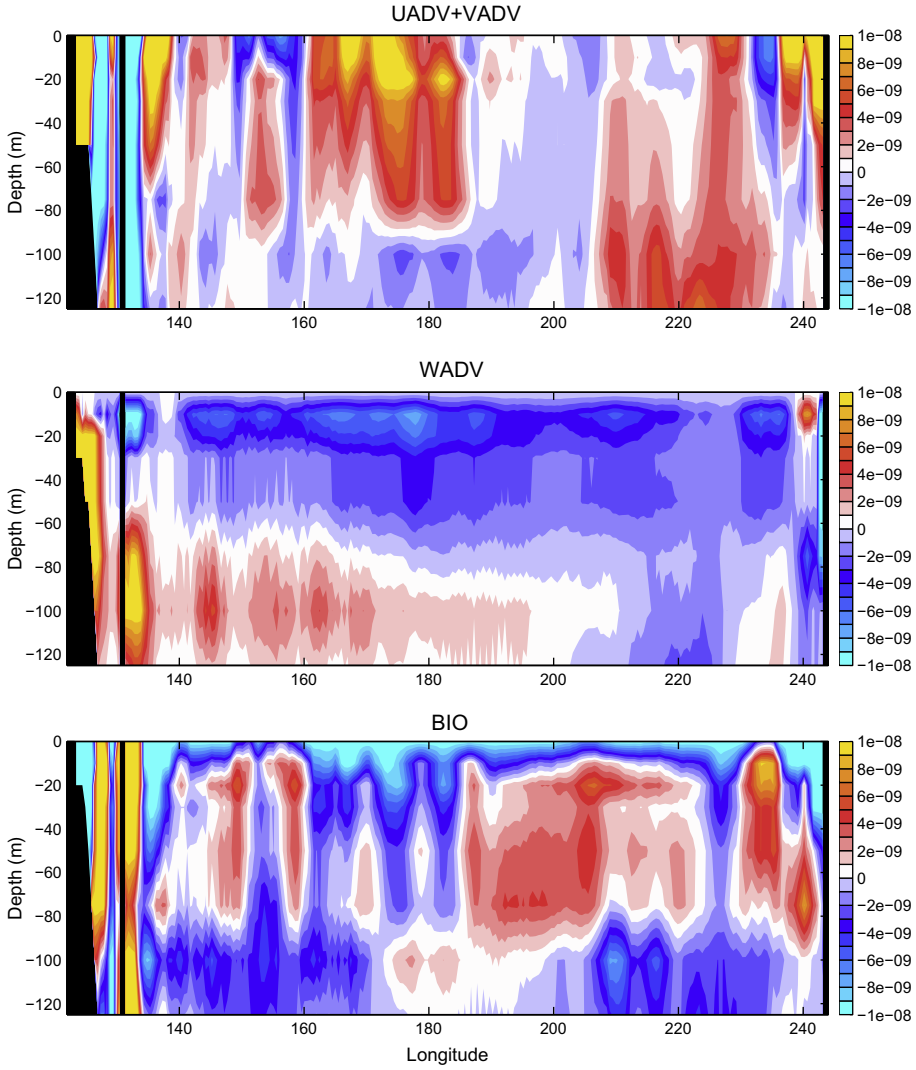

Fig. 17. Sections along 30°N depicting the vertical structures of annual-mean advection and biology terms contributing to CDOM dynamics.

In the biogeochemical model, the BIO is determined by source and sink terms. The source terms include phytoplankton excretion and zooplankton feeding loss, and the sink terms are composed of bacteria uptake and photolysis by UV light. For the entire euphotic zone in the HW region, seasonal variation of the BIO follows closely with change in phytoplankton excretion, and in bacteria uptake with seasonal peaks between spring and summer (Fig. 15). Zooplankton feeding loss and photolysis stay relatively constant over the two-year period. When averaged over time, two dominant terms in the annual-mean BIO are phytoplankton excretion and bacteria uptake that are significantly higher than the contributions from zooplankton feeding loss and photolysis, as UV light is intense mostly in the upper layer, while bacteria uptake generally takes place throughout the euphotic zone (Fig. 16).

The zonal transection along 30°N further depicts the vertical structures of the annual-mean terms contributing to the CDOM dynamics (Fig. 17). Both horizontal and vertical advections, as well as the BIO term, are considerably stronger in the coastal regions relative to the central basin. Horizontal advections are shown to be highly variable in both horizontal and vertical directions, while vertical advection shows a relatively coherent feature with negative values above 70 m and positive values below, except for the region around 140°W where negative values exist in the entire euphotic zone. Due to the photolysis by UV light, the BIO term illustrates large negative values in the upper layer and varies in depth across the transection. Away from the surface layer, negative BIO values, especially those generally found at the bottom of the euphotic zone, are primarily attributable to bacteria uptake. On the other hand, the BIO source terms, including phytoplankton and zooplankton contributions, are more distinct in the middle of the euphotic zone with clear spatial variability across this transection. This suggests CDOM dynamics are highly variable in space, which is induced by the variability in both physical and biological processes.

Physical process affecting biological properties such as phytoplankton chlorophyll via (horizontal and vertical) transports of nutrients, and sometimes the chlorophyll itself, has been widely accepted as the concept of how physics changes biology in the ocean. However, when considering ocean optics, another mechanism becomes possible: physical transport of CDOM changes water optical properties, which can further modify underwater light field and subsequently affect phytoplankton chlorophyll. Positive transport of CDOM can increase water optical properties, increase light attenuation, decrease underwater PAR values, and eventually decrease local chlorophyll concentration. This mechanism is different from the one where positive transport of nutrients or chlorophyll usually

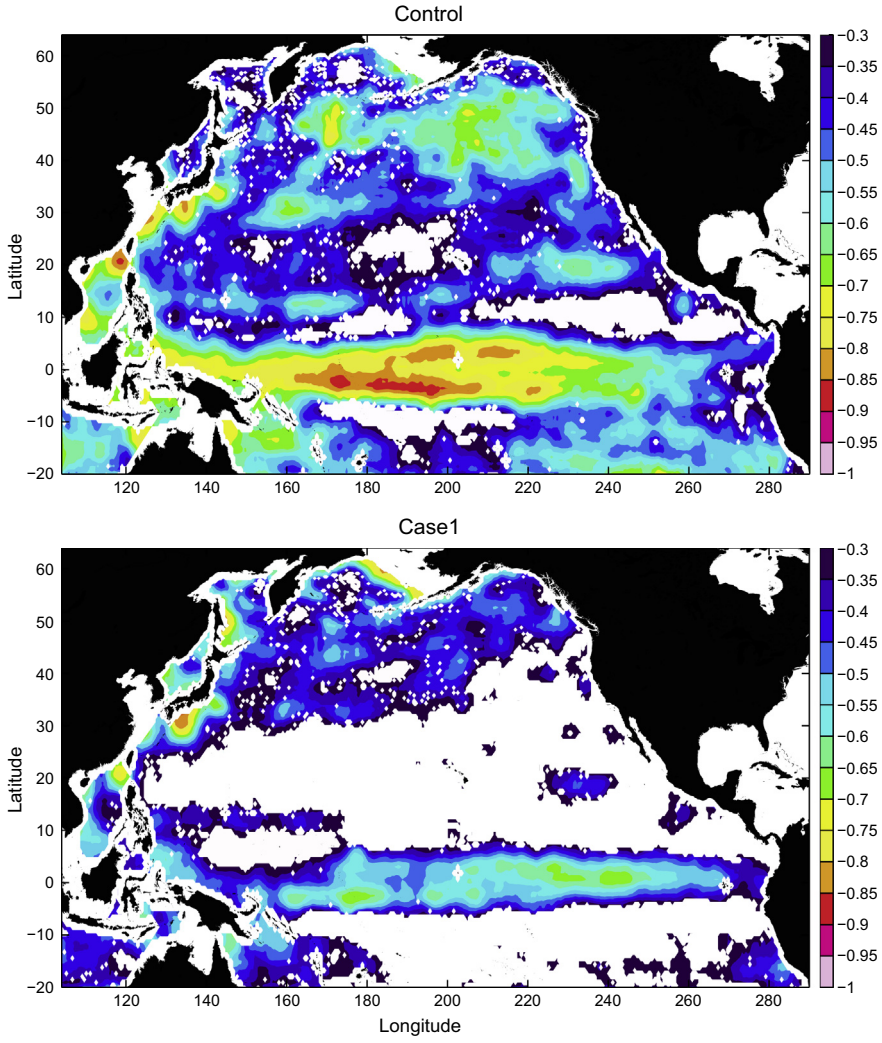

Fig. 18. Correlation coefficients between horizontal advection term (LADV) and BIO term for CDOM dynamics using two-year time series (2006 and 2007) for Control and Case1. A two-week high-frequency-pass filter was applied prior to the correlation calculation.

leads to an increase of local biomass. To illustrate this mechanism, correlation coefficients between horizontal advection term (LADV) and BIO term for CDOM are calculated (Fig. 18). As the BIO tends to dominate the seasonal cycle of the local CDOM concentration, a two-week high-frequency-pass filter is applied for the horizontal advection and BIO before the correlation is calculated. In Case1 where light is only controlled by phytoplankton, advection of CDOM does not change underwater PAR and subsequent BIO CDOM. However, there is still significant negative correlation between LADV and BIO in the equatorial Pacific and most of the North Pacific. This is likely related to the photolysis by UV light in the BIO calculation, in which positive LADV CDOM increases local CDOM concentration that can increase photolysis and consequently decrease BIO CDOM. In the control run where light attenuation by CDOM is considered, the correlation coefficient between LADV and BIO systematically increases compared to that in Case1, especially in the subtropics where the correlation is not significant in Case1. This high negative correlation generally presents over the entire basin, implying optical modulation of physical–biological interactions. Without explicitly representing CDOM dynamics in the biogeochemical model, this effect is often ignored by many studies. Here, we only show the influence of physical transport of CDOM on biological process, as we do not include its biological feedback to physical properties in the model. If we considered this feedback, we could expect the modification of water temperature by physical transport of CDOM, because LADV of CDOM can change both underwater PAR (400–700 nm) and shortwave radiation (usually in 400–1000 nm) that heats the upper ocean.

4. Discussion and conclusions

Satellite-observed CDOM generally shows different spatial distribution patterns from chlorophyll, attributable to distinct source and sink processes (Nelson and Siegel, 2013). This creates estimation errors for empirical chlorophyll retrieval algorithms, say OC4V4, which assumes a fixed relationship between chlorophyll and CDOM concentrations. These errors, without proper constraints, could manifest in the assessment of ocean carbon cycling. For example, Siegel et al. (2005) calculated a global net primary production of 53.5 Gt C y^{-1} based on OC4V4-derived chlorophyll concentration; this number is reduced to 37.1 Gt C y^{-1} when using the chlorophyll concentration from a semi-analytical algorithm based on independent CDOM calculations. With different chlorophyll retrieval algorithms, the discrepancy between these calculations is uncertain, but it suggests that the potential impact of CDOM on ecosystem processes and functions may not be trivial.

As indicated by Siegel et al. (2005), without accurately separating in-water constituents, interpretations of ocean color data (e.g., seasonal analysis, trend detection) could be easily confounded by uncertainties, especially due to the nonlinear relationship between CDOM and chlorophyll. Our study confirms that CDOM dynamics should be explicitly considered in biogeochemical models, as it can feed back to the whole marine system including physics, optics, and biogeochemistry.

Currently, coupled ecosystem models typically use sophisticated thermodynamics, fairly sophisticated biology, but grossly simplified underwater light attenuation. Models used for global-scale predictions of climate change as well as for understanding the global ocean–atmosphere system are often driven by simple analytical formulations of light penetration through the water column. A lot of efforts have been made to improve model resolution and the dynamics of physical and biological model components. In contrast, the uncertainty induced by the oversimplified treatment of light has rarely been discussed. The difference between Control and Case1 suggests that this uncertainty cannot be ignored. It not only changes underwater light condition but also alters distributions of phytoplankton chlorophyll and nutrient levels, and tends to be more significant in the subsurface, which could potentially affect the efficiency and structure of the biological pump and carbon cycling.

To summarize, a new biogeochemical model consisting of 31 state variables has been developed and coupled to a 3-D physical model in the Pacific Ocean. With the explicitly represented DOM pool, this new model is able to link key biogeochemical processes with optical processes. Moreover, the inclusion of optical processes allows direct comparison between model and satellite-derived optical data, which gives additional constraints on model parameters to reduce uncertainties in model simulations. The development of this new model and parameter tuning rely on various modeling approaches, such as phytoplankton photoacclimation, CDOM dynamics, microbial loop, optics conversion, among others, based on previous studies (e.g., Anderson and Williams, 1998; Geider et al., 1998; Bissett et al., 1999a; Chai et al., 2002; Moore et al., 2002;Fujii et al., 2007). In practice, it is difficult to model an entire ocean basin with a wide range of biological provinces and diverse phytoplankton communities using only one set of model parameters. Nevertheless, model validation against satellite and in situ data appears to show that the model is flexible enough to reproduce general biogeochemical and optical features observed.

The main advantage of the coupled model is that it combines physical, biogeochemical, and optical processes. Our results demonstrate the importance of CDOM in regulating underwater light field and subsequent biological activities. Our analysis suggests that the inclusion of CDOM in the ecosystem model could substantially affect biological processes. Without CDOM attenuating light, modeled depth-integrated PP is about 10% higher than that in the control run over the entire Pacific basin. Moreover, this discrepancy is highly variable in space with magnitudes reaching higher than 100% in some locations. The coupled model demonstrates that the physical transport of CDOM can change water optical properties, which can further modify underwater light field and subsequently affect the distribution of phytoplankton chlorophyll. This mechanism is different from the one where transport of nutrients and/or chlorophyll usually leads to an increase of local biomass. One potential for this coupled model is to assimilate satellite-sensed or in situ optical data directly in addition to chlorophyll concentration. This will increase the realism of ecosystem simulations for better prediction and monitoring of biological conditions (e.g., harmful algal blooms) in open oceans and coastal regions.

Acknowledgements

This research was supported by NASA grants (NNG04GM64G and NNX09AU39G) to F. Chai. The authors wish to thank the SeaWiFS Project for providing the SeaWiFS data (http://oceancolor.gsfc.nasa.gov/), and the editor and three anonymous reviewers for their valuable comments.

Appendix A

A.1. Governing equations

The model equations describing individual compartments all take the form:

$$\frac{\partial B_i}{\partial t} = \mathrm{PHY}(B_i) + \mathrm{BIO}(B_i). \tag{A1}$$

The model state variables, B_i, represent picoplankton (P1 (mmolN m^{-3}), C1 (mmolC m^{-3}), and Chl1 (mgChl m^{-3})), diatoms (P2 (mmolN m^{-3}), C2 (mmolC m^{-3}), and Chl2 (mgChl m^{-3})), coccolithophorids (P3 (mmolN m^{-3}), C3 (mmolC m^{-3}), and Chl3 (mgChl m^{-3})), microzooplankton (Z1 (mmolN m^{-3}), ZC1 (mmolC m^{-3})), mesozooplankton (Z2 (mmolN m^{-3}), ZC2 (mmolC m^{-3})), bacteria nitrogen (BAC (mmolN m^{-3})), detritus (PON (mmolN m^{-3}), POC (mmolC m^{-3})), biogenic silicate ($bSiO_2$ (mmolSi m^{-3})), calcium carbonate (PIC (mmolC m^{-3})), labile DON (LDON (mmolN m^{-3})), labile DOC (LDOC (mmolC m^{-3})), semi-labile DON (SDON (mmolN m^{-3})), semi-labile DOC (SDOC (mmolC m^{-3})), colored labile DOC (CLDOC (mmolC m^{-3})), colored semi-labile DOC (CSDOC (mmolC m^{-3})), dissolved oxygen (DO (mmolO m^{-3})), dissolved inorganic nutrients (NO_3 (mmolN m^{-3}), NH_4 (mmolN m^{-3}), PO_4 (mmolP m^{-3}), SiO_4 (mmolSi m^{-3})), total alkalinity (TALK (mmol m^{-3})), and total CO_2 (TCO_2 (mmolC m^{-3})).

The term $\mathrm{PHY}(B_i)$ represents the contribution to concentration change due to physical processes. The term $\mathrm{BIO}(B_i)$ represents biological sources and sinks of a particular compartment. The $\mathrm{BIO}(B_i)$ terms in the model are:

$$\mathrm{BIO(P1)} = \underbrace{(1-\varepsilon_1)\mathrm{PP1}}_{growth} - \underbrace{G_1}_{grazing\ by\ Z1} - \underbrace{\gamma_3 \mathrm{P1}}_{mortality}, \tag{A2}$$

$$\mathrm{BIO(C1)} = \underbrace{(1-\varepsilon_1)\mathrm{NPC1}}_{growth} - \underbrace{G_1 \times \frac{\mathrm{C1}}{\mathrm{P1}}}_{grazing\ by\ Z1} - \underbrace{\gamma_3 \mathrm{C1}}_{mortality}, \tag{A3}$$

$$\mathrm{BIO(Chl1)} = \underbrace{\rho_{\mathrm{Chl1}}(1-\varepsilon_1)\mathrm{PP1}}_{growth} - \underbrace{G_1 \times \frac{\mathrm{Chl1}}{\mathrm{P1}}}_{grazing\ by\ Z1} - \underbrace{\gamma_3 \mathrm{Chl1}}_{mortality}, \tag{A4}$$

$$\mathrm{BIO(P2)} = \underbrace{(1-\varepsilon_2)\mathrm{PP2}}_{growth} - \underbrace{G_2}_{grazing\ by\ Z2} - \underbrace{\gamma_4 \mathrm{P2}}_{mortality} - \underbrace{\frac{\partial}{\partial z}(W_1 \mathrm{P2})}_{\text{sin king}}, \tag{A5}$$

$$\mathrm{BIO(C2)} = \underbrace{(1-\varepsilon_2)\mathrm{NPC2}}_{growth} - \underbrace{G_2 \times \frac{\mathrm{C2}}{\mathrm{P2}}}_{grazing\ by\ Z2} - \underbrace{\gamma_4 \mathrm{C2}}_{mortality} - \underbrace{\frac{\partial}{\partial z}(W_1 \mathrm{C2})}_{\text{sin king}}, \tag{A6}$$

$$\mathrm{BIO(Chl2)} = \underbrace{\rho_{\mathrm{Chl2}}(1-\varepsilon_2)\mathrm{PP2}}_{growth} - \underbrace{G_2(z) \times \frac{\mathrm{Chl2}}{\mathrm{P2}}}_{grazing\ by\ Z2} - \underbrace{\gamma_4 \mathrm{Chl2}}_{mortality} - \underbrace{\frac{\partial}{\partial z}(W_1 \mathrm{Chl2})}_{\text{sin king}}, \tag{A7}$$

$$\mathrm{BIO(P3)} = \underbrace{(1-\varepsilon_3)\mathrm{PP3}}_{growth} - \underbrace{G_5}_{grazing\ by\ Z2} - \underbrace{\gamma_{10} \mathrm{P3}}_{mortality} - \underbrace{\frac{\partial}{\partial z}(W_3 \mathrm{P3})}_{\text{sin king}}, \tag{A8}$$

$$\mathrm{BIO(C3)} = \underbrace{(1-\varepsilon_3)\mathrm{NPC3}}_{growth} - \underbrace{G_5 \times \frac{\mathrm{C3}}{\mathrm{P3}}}_{grazing\ by\ Z2} - \underbrace{\gamma_{10}\mathrm{C3}}_{mortality} - \underbrace{\frac{\partial}{\partial z}(W_3\mathrm{C3})}_{\sin king}, \tag{A9}$$

$$\mathrm{BIO(Chl3)} = \underbrace{\rho_{Chl3}(1-\varepsilon_3)\mathrm{PP3}}_{growth} - \underbrace{G_5 \times \frac{\mathrm{Chl3}}{\mathrm{P3}}}_{grazing\ by\ Z2} - \underbrace{\gamma_{10}\mathrm{Chl3}}_{mortality} - \underbrace{\frac{\partial}{\partial z}(W_3\mathrm{Chl3})}_{\sin king}, \tag{A10}$$

$$\mathrm{BIO(Z1)} = \underbrace{\gamma_1(1-\phi_1)(G_1+G_6)}_{grazing} - \underbrace{G_3}_{predation\ by\ Z2} - \underbrace{reg_1\mathrm{Z1}}_{excretion}, \tag{A11}$$

$$\mathrm{BIO(ZC1)} = \underbrace{\gamma_1(1-\phi_1)\left(G_1\frac{\mathrm{C1}}{\mathrm{P1}} + R_B G_6\right)}_{grazing} - \underbrace{G_3\frac{\mathrm{ZC1}}{\mathrm{Z1}}}_{predation\ by\ Z2} - \underbrace{reg_1\mathrm{ZC1}}_{excretion}, \tag{A12}$$

$$\mathrm{BIO(Z2)} = \underbrace{\gamma_2(1-\phi_2)(G_2+G_3+G_4+G_5)}_{grazing} - \underbrace{reg_2\mathrm{Z2}}_{excretion} - \underbrace{\lambda\mathrm{Z2}^2}_{loss}, \tag{A13}$$

$$\mathrm{BIO(ZC2)} = \underbrace{\gamma_{22}(1-\phi_2)\left(G_2\frac{\mathrm{C2}}{\mathrm{P2}} + G_3\frac{\mathrm{ZC1}}{\mathrm{Z1}} + G_4\frac{\mathrm{POC}}{\mathrm{PON}} + G_5\frac{\mathrm{C3}}{\mathrm{P3}}\right)}_{grazing} - \underbrace{reg_2\mathrm{ZC2}}_{excretion} - \underbrace{\lambda\mathrm{ZC2}^2}_{loss}, \tag{A14}$$

$$\mathrm{BIO(NH_4)} = -\underbrace{\mathrm{RP1}}_{uptake\ by\ P1} - \underbrace{\mathrm{RP2}}_{uptake\ by\ P2} - \underbrace{\mathrm{RP3}}_{uptake\ by\ P3} + \underbrace{reg_1\mathrm{Z1} + reg_2\mathrm{Z2}}_{Z1,\ Z2\ excretion} + \underbrace{0.9D_{\mathrm{PON}}\mathrm{PON}}_{\mathrm{PON}\ remineralization} - \underbrace{\gamma_7\mathrm{NH_4}}_{nitrification} + \underbrace{E_B}_{\mathrm{BAC}\ remineralization}, \tag{A15}$$

$$\mathrm{BIO(SiO_4)} = -\underbrace{\mathrm{USiO_4}}_{silicification} + \underbrace{D_{\mathrm{Si}} \times \mathrm{bSiO_2}}_{remineralization}, \tag{A16}$$

$$\mathrm{BIO(NO_3)} = -\underbrace{\mathrm{NP1}}_{uptake\ by\ P1} - \underbrace{\mathrm{NP2}}_{uptake\ by\ P2} - \underbrace{\mathrm{NP3}}_{uptake\ by\ P3} + \underbrace{\gamma_7\mathrm{NH_4}}_{nitrification}, \tag{A17}$$

$$\mathrm{BIO}(PO_4) = R_{\mathrm{PN}}\left(-\underbrace{\mathrm{PP1}-\mathrm{PP2}-\mathrm{PP3}}_{uptake\ by\ phytoplankton} + \underbrace{reg_1\mathrm{Z1} + reg_2\mathrm{Z2}}_{Z1,\ Z2\ excretion} + \underbrace{0.9D_{\mathrm{PON}}\mathrm{PON}}_{\mathrm{PON}\ remineralization} + \underbrace{E_B}_{\mathrm{BAC}\ remineralization}\right), \tag{A18}$$

$$\mathrm{BIO(bSiO_2)} = \mathrm{Si2N} \times \left(\underbrace{G_2}_{fecal\ pellet} + \underbrace{\gamma_4\mathrm{P2}}_{\mathrm{P2}\ mortality}\right) - \underbrace{D_{\mathrm{Si}} \times \mathrm{bSiO_2}}_{remineralization} - \underbrace{\frac{\partial}{\partial z}(W_4\mathrm{bSiO_2})}_{\sin king}, \tag{A19}$$

$$\mathrm{BIO(PIC)} = R_{\mathrm{CaC}}\left(\underbrace{G_5\frac{\mathrm{C3}}{\mathrm{P3}}}_{fecal\ pellet} + \underbrace{\gamma_{10}\mathrm{C3}}_{\mathrm{P3}\ mortality}\right) - \underbrace{D_{\mathrm{PIC}}\mathrm{PIC}}_{dissolution} - \underbrace{\frac{\partial}{\partial z}(W_5\mathrm{PIC})}_{\sin king}, \tag{A20}$$

$$\mathrm{BIO(PON)} = \underbrace{(1-\gamma_2)(1-\phi_2)(G_2+G_3+G_4+G_5)}_{fecal\ pellet\ by\ Z2} + \underbrace{(1-\gamma_1)(1-\phi_1)(G_1+G_6)}_{fecal\ pellet\ by\ Z1} - \underbrace{G_4}_{Z2\ grazing} + \underbrace{\gamma_3(1-\delta_1)\mathrm{P1}}_{\mathrm{P1}\ mortality} + \underbrace{\gamma_4(1-\delta_2)\mathrm{P2}}_{\mathrm{P2}\ mortality} + \underbrace{\gamma_{10}(1-\delta_3)\mathrm{P3}}_{\mathrm{P3}\ mortality} - \underbrace{0.9D_{\mathrm{PON}}\mathrm{PON}}_{remineralization} - \underbrace{0.1D_{\mathrm{PON}}\mathrm{PON}}_{detritus\ breakdown} - \underbrace{\frac{\partial}{\partial z}(W_6\mathrm{PON})}_{\sin king}, \tag{A21}$$

$$\mathrm{BIO(POC)} = \underbrace{(1-\gamma_{22})(1-\phi_2)\left(G_2\frac{\mathrm{C2}}{\mathrm{P2}} + G_3\frac{\mathrm{ZC1}}{\mathrm{Z1}} + G_4\frac{\mathrm{POC}}{\mathrm{PON}} + G_5\frac{\mathrm{C3}}{\mathrm{P3}}\right)}_{fecal\ pellet\ by\ Z2} + \underbrace{(1-\gamma_1)(1-\phi_1)\left(G_1\frac{\mathrm{C1}}{\mathrm{P1}} + R_B G_6\right)}_{fecal\ pellet\ by\ Z1} - \underbrace{G_4(z)\frac{\mathrm{POC}}{\mathrm{PON}}}_{grazing\ by\ Z2} + \underbrace{\gamma_3(1-\delta_1)\mathrm{C1}}_{\mathrm{P1}\ mortality} + \underbrace{\gamma_4(1-\delta_2)\mathrm{C2}}_{\mathrm{P2}\ mortality} + \underbrace{\gamma_{10}(1-\delta_3)\mathrm{C3}}_{\mathrm{P3}\ mortality} - \underbrace{0.9D_{\mathrm{PON}}\mathrm{POC}}_{\mathrm{POC}\ remineralization} - \underbrace{0.1D_{\mathrm{PON}}\mathrm{POC}}_{detritus\ breakdown} - \underbrace{\frac{\partial}{\partial z}(W_7\mathrm{POC})}_{\sin king}, \tag{A22}$$

$$\mathrm{BIO(LDON)} = \underbrace{\varepsilon_1\mathrm{PP1} + \varepsilon_2\mathrm{PP2} + \varepsilon_3\mathrm{PP3}}_{phytoplankton\ exudation} + \beta_1\left[\underbrace{\phi_1(G_1+G_6) + \phi_2(G_2+G_3+G_4+G_5)}_{zooplankton\ messy\ feeding} + \underbrace{\delta_1\gamma_3\mathrm{P1} + \delta_2\gamma_4\mathrm{P2} + \delta_3\gamma_{10}\mathrm{P3}}_{phytoplankton\ mortality} + \underbrace{\gamma_{12}\mathrm{BAC}}_{bacteria\ mortality} + \underbrace{0.1D_{\mathrm{PON}}\mathrm{PON}}_{detritus\ breakdown}\right] - \underbrace{U_N}_{bacteria\ uptake} + \underbrace{\gamma_{13}\frac{\mathrm{BAC}\times\mathrm{SDON}}{K_{\mathrm{SDON}}+\mathrm{SDON}}}_{breakdown\ of\ SDON}, \tag{A23}$$

$$\mathrm{BIO(SDON)} = \underbrace{(1-\beta_1)[\phi_1(G_1+G_6) + \phi_2(G_2+G_3+G_4+G_5)}_{zooplankton\ messy\ feeding} + \underbrace{\delta_1\gamma_3\mathrm{P1} + \delta_2\gamma_4\mathrm{P2} + \delta_3\gamma_{10}\mathrm{P3}}_{phytoplankton\ mortality} + \underbrace{\gamma_{12}\mathrm{BAC}}_{bacteria\ mortality} + \underbrace{0.1D_{\mathrm{PON}}\mathrm{PON}}_{detritus\ breakdown}] - \underbrace{\gamma_{13}\frac{\mathrm{BAC}\times\mathrm{SDON}}{K_{\mathrm{SDON}}+\mathrm{SDON}}}_{breakdown\ of\ SDON}, \tag{A24}$$

$$\mathrm{BIO(LDOC)} = \underbrace{(1-\mathrm{colorFR1})[\varepsilon_1(1-\varepsilon_4)\mathrm{NPC1} + \varepsilon_2(1-\varepsilon_5)\mathrm{NPC2} + \varepsilon_3(1-\varepsilon_6)\mathrm{NPC3}}_{phytoplankton\ exudation} + \beta_1\underbrace{\left(\phi_1\left(G_1\frac{\mathrm{C1}}{\mathrm{P1}} + R_B G_6\right) + \phi_2\left(G_2\frac{\mathrm{C2}}{\mathrm{P2}} + G_3\frac{\mathrm{ZC1}}{\mathrm{Z1}} + G_4\frac{\mathrm{POC}}{\mathrm{PON}} + G_5\frac{\mathrm{C3}}{\mathrm{P3}}\right)\right)}_{zooplankton\ messy\ feeding} + \beta_2\underbrace{(\varepsilon_1\varepsilon_4\mathrm{NPC1} + \varepsilon_2\varepsilon_5\mathrm{NPC2} + \varepsilon_3\varepsilon_6\mathrm{NPC3})}_{extra\ photosynthetic\ carbon} + \beta_1(\underbrace{\delta_1\gamma_3\mathrm{C1} + \delta_2\gamma_4\mathrm{C2} + \delta_3\gamma_{10}\mathrm{C3}}_{phytoplankton\ mortality} + \underbrace{\gamma_{12}R_B\mathrm{BAC}}_{bacteria\ mortality} + \underbrace{0.1D_{\mathrm{PON}}\mathrm{POC}}_{detritus\ breakdown})] - \underbrace{\beta_3(F_B R_B + S_B)}_{bacteria\ uptake} + \underbrace{\gamma_{13}\frac{R_B\mathrm{BAC}\times\mathrm{SDOC}}{K_{\mathrm{SDOC}}+\mathrm{SDOC}}}_{breakdown\ of\ SDOC} + \underbrace{\mathrm{UVLDOC} + \mathrm{UVSDOC}}_{UV\ photolysis}, \tag{A25}$$

$$\begin{aligned}\mathrm{BIO(SDOC)} = {} & \underbrace{(1-\beta_1)(1-\mathrm{colorFR2})\left[\phi_1\left(G_1\frac{\mathrm{C1}}{\mathrm{P1}}+R_BG_6\right)+\phi_2\left(G_2\frac{\mathrm{C2}}{\mathrm{P2}}+G_3\frac{\mathrm{ZC1}}{\mathrm{Z1}}+G_4\frac{\mathrm{POC}}{\mathrm{PON}}+G_5\frac{\mathrm{C3}}{\mathrm{P3}}\right)\right]}_{\textit{zooplankton messy feeding}} \\ & + \underbrace{(1-\beta_2)(1-\mathrm{colorFR2})(\varepsilon_1\varepsilon_4\mathrm{NPC1}+\varepsilon_2\varepsilon_5\mathrm{NPC2}+\varepsilon_3\varepsilon_6\mathrm{NPC3})}_{\textit{extra photosynthetic carbon}}+(1-\beta_1)(1-\mathrm{colorFR2}) \\ & \times(\underbrace{\delta_1\gamma_3\mathrm{C1}+\delta_2\gamma_4\mathrm{C2}+\delta_3\gamma_{10}\mathrm{C3}}_{\textit{phytoplankton mortality}}+\underbrace{\gamma_{12}R_B\mathrm{BAC}}_{\textit{bacteria mortality}}+\underbrace{0.1D_{\mathrm{PON}}\mathrm{POC}}_{\mathrm{det}\textit{ritus breakdown}})-\underbrace{\gamma_{13}\frac{R_B\mathrm{BAC}\times\mathrm{SDOC}}{K_{\mathrm{SDOC}}+\mathrm{SDOC}}}_{\textit{breakdown of SDOC}},\end{aligned} \tag{A26}$$

$$\mathrm{BIO(BAC)} = \underbrace{F_B}_{\textit{uptake DOM}} - \underbrace{G_6}_{\textit{grazing by Z1}} - \underbrace{\gamma_{12}\mathrm{BAC}}_{\textit{mortality}}, \tag{A27}$$

$$\begin{aligned}\mathrm{BIO(CLDOC)} = {} & \underbrace{\mathrm{colorFR1}[\varepsilon_1(1-\varepsilon_4)\mathrm{NPC1}+\varepsilon_2(1-\varepsilon_5)\mathrm{NPC2}+\varepsilon_3(1-\varepsilon_6)\mathrm{NPC3}}_{\textit{phytoplankton exudation}} \\ & +\beta_2(\underbrace{\varepsilon_1\varepsilon_4\mathrm{NPC1}+\varepsilon_2\varepsilon_5\mathrm{NPC2}+\varepsilon_3\varepsilon_6\mathrm{NPC3}}_{\textit{extra photosynthetic carbon}}) \\ & +\underbrace{\beta_1\left(\phi_1\left(G_1\frac{\mathrm{C1}}{\mathrm{P1}}+R_BG_6\right)+\phi_2\left(G_2\frac{\mathrm{C2}}{\mathrm{P2}}+G_3\frac{\mathrm{ZC1}}{\mathrm{Z1}}+G_4\frac{\mathrm{POC}}{\mathrm{PON}}+G_5\frac{\mathrm{C3}}{\mathrm{P3}}\right)\right)}_{\textit{zooplankton messy feeding}} \\ & +\beta_1(\underbrace{\delta_1\gamma_3\mathrm{C1}+\delta_2\gamma_4\mathrm{C2}+\delta_3\gamma_{10}\mathrm{C3}}_{\textit{phytoplankton mortality}}+\underbrace{\gamma_{12}R_B\mathrm{BAC}}_{\textit{bacteria mortality}}+\underbrace{0.1D_{\mathrm{PON}}\mathrm{POC}}_{\mathrm{det}\textit{ritus breakdown}})] \\ & -\underbrace{\mathrm{UVLDOC}-\mathrm{UVLDIC}}_{\textit{UV photolysis}}-\underbrace{(1-\beta_3)(F_BR_B+S_B)}_{\textit{bacteria uptake}},\end{aligned} \tag{A28}$$

$$\begin{aligned}\mathrm{BIO(CSDOC)} = {} & \mathrm{colorFR2}(1-\beta_1) \\ & \underbrace{\left[\phi_1\left(G_1\frac{\mathrm{C1}}{\mathrm{P1}}+R_BG_6\right)+\phi_2\left(G_2\frac{\mathrm{C2}}{\mathrm{P2}}+G_3\frac{\mathrm{ZC1}}{\mathrm{Z1}}+G_4\frac{\mathrm{POC}}{\mathrm{PON}}+G_5\frac{\mathrm{C3}}{\mathrm{P3}}\right)\right]}_{\textit{zooplankton messy feeding}} \\ & +\mathrm{colorFR2}(1-\beta_2)(\underbrace{\varepsilon_1\varepsilon_4\mathrm{NPC1}+\varepsilon_2\varepsilon_5\mathrm{NPC2}+\varepsilon_3\varepsilon_6\mathrm{NPC3}}_{\textit{extra photosynthetic carbon}}) \\ & +\mathrm{colorFR2}(1-\beta_1)(\underbrace{\delta_1\gamma_3\mathrm{C1}+\delta_2\gamma_4\mathrm{C2}+\delta_3\gamma_{10}\mathrm{C3}}_{\textit{phytoplankton mortality}}+\underbrace{\gamma_{12}R_B\mathrm{BAC}}_{\textit{bacteria mortality}} \\ & +\underbrace{0.1D_{\mathrm{PON}}\mathrm{POC}}_{\mathrm{det}\textit{ritus breakdown}})-\underbrace{\mathrm{UVSDOC}-\mathrm{UVSDIC}}_{\textit{UV photolysis}},\end{aligned} \tag{A29}$$

$$\begin{aligned}\mathrm{BIO(TCO_2)} = {} & \underbrace{D_{\mathrm{PIC}}\mathrm{PIC}}_{\mathrm{PIC}\ \textit{dissolution}} - \underbrace{R_{\mathrm{CaC}}(1-\varepsilon_3)\mathrm{NPC3}}_{\textit{calcification}} \\ & -\underbrace{[(1-\varepsilon_1)\mathrm{NPC1}+(1-\varepsilon_2)\mathrm{NPC2}+(1-\varepsilon_3)\mathrm{NPC3}]}_{\textit{phytoplankton growth}} \\ & +\underbrace{S_B}_{\textit{bacteria respiration}}+\underbrace{(reg_1\mathrm{ZC1}+reg_2\mathrm{ZC2})}_{\textit{excretion}} \\ & +\underbrace{0.9D_{\mathrm{PON}}\mathrm{POC}}_{\mathrm{POC}\ \mathit{re}\mathrm{min}\mathit{eralization}}+\underbrace{\mathrm{UVLDIC}+\mathrm{UVSDIC}}_{\textit{UV photolysis}},\end{aligned} \tag{A30}$$

$$\begin{aligned}\mathrm{BIO(TALK)} = {} & 2.0\times[\underbrace{D_{\mathrm{PIC}}\mathrm{PIC}}_{\mathrm{PIC}\ \textit{dissolution}} - \underbrace{R_{\mathrm{CaC}}(1-\varepsilon_3)\mathrm{NPC3}}_{\textit{calcification}}] \\ & +\underbrace{(\mathrm{NP1}+\mathrm{NP2}+\mathrm{NP3})}_{\textit{phytoplankton growth}}-\underbrace{\gamma_7\mathrm{NH_4}}_{\textit{nitrification}} \\ & -\underbrace{(\mathrm{RP1}+\mathrm{RP2}+\mathrm{RP3})}_{\textit{uptake by phytoplankton}}+\underbrace{reg_1\mathrm{Z1}+reg_2\mathrm{Z2}}_{\textit{excretion}} \\ & +\underbrace{0.9D_{\mathrm{PON}}\mathrm{PON}}_{\mathit{re}\mathrm{min}\mathit{eralization}}-\underbrace{\gamma_7\mathrm{NH_4}}_{\textit{nitrification}}+\underbrace{E_B}_{\mathrm{BAC}\ \mathit{re}\mathrm{min}\mathit{eralization}},\end{aligned} \tag{A31}$$

$$\begin{aligned}\mathrm{BIO(DO)} = {} & R_{o2no3}\underbrace{(\mathrm{NP1}+\mathrm{NP2}+\mathrm{NP3})}_{\textit{phytoplankton growth}}+R_{o2nh4}(\mathrm{RP1}+\mathrm{RP2}+\mathrm{RP3}) \\ & -2.0\times\underbrace{\gamma_7\mathrm{NH_4}}_{\textit{nitrification}}-R_{o2nh4}\left(\underbrace{reg_1\mathrm{Z1}+reg_2\mathrm{Z2}}_{\textit{excretion}}\right. \\ & \left.+\underbrace{0.9D_{\mathrm{PON}}\mathrm{PON}}_{\mathit{re}\mathrm{min}\mathit{eralization}}+\underbrace{E_B}_{\mathrm{BAC}\ \mathit{re}\mathrm{min}\mathit{eralization}}\right).\end{aligned} \tag{A32}$$

A.2. Formulation of individual processes

Nutrients uptake by picoplankton:

$$\begin{aligned}\mathrm{NP1} = {} & V_N^C ref_{\mathrm{P1}}\times\frac{1-fnit_{\mathrm{P1}}}{1.015-fnit_{\mathrm{P1}}}\times Tfunc\times\frac{\mathrm{NO_3}}{K_{\mathrm{P1\_NO_3}}+\mathrm{NO_3}} \\ & \times e^{-\Psi_1\mathrm{NH_4}}\times\left\{1-\exp\left(\frac{-\alpha\times\theta^{\mathrm{C1}}\times\mathrm{PAR}}{P_{ref}^{\mathrm{C1}}\times fnit_{\mathrm{P1}}\times Tfunc}\right)\right\} \\ & \times\mathrm{C1},\end{aligned} \tag{A33}$$

$$V_{\mathrm{N}}^{C} ref_{\mathrm{P1}} = P_{ref}^{\mathrm{C1}}\times Q_{\max}, \tag{A34}$$

$$fnit_{\mathrm{P1}} = \frac{uQ1-Q_{\min}}{Q_{\max}-Q_{\min}}, \tag{A35}$$

$$uQ1 = \frac{\mathrm{P1}}{\mathrm{C1}},\quad Q_{\min}<uQ1<Q_{\max}, \tag{A36}$$

$$\theta^{\mathrm{C1}} = \frac{\mathrm{Chl1}}{\mathrm{C1}}, \tag{A37}$$

$$Tfunc = \exp\left\{-4000\times\left(\frac{1}{T+273.15}-\frac{1}{303.15}\right)\right\}, \tag{A38}$$

$$\begin{aligned}\mathrm{RP1} = {} & V_N^C ref_{\mathrm{P1}}\times\frac{1-fnit_{\mathrm{P1}}}{1.015-fnit_{\mathrm{P1}}}\times Tfunc\times\frac{\mathrm{NH_4}}{K_{\mathrm{P1\_NH_4}}+\mathrm{NH_4}} \\ & \times\left\{1-\exp\left(\frac{-\alpha\times\theta^{\mathrm{C1}}\times\mathrm{PAR}}{P_{ref}^{\mathrm{C1}}\times fnit_{\mathrm{P1}}\times Tfunc}\right)\right\}\times\mathrm{C1},\end{aligned} \tag{A39}$$

$$\mathrm{PP1} = \mathrm{NP1}+\mathrm{RP1}. \tag{A40}$$

Carbon uptake by picoplankton:

$$\begin{aligned}P^{\mathrm{C1}} = {} & P_{ref}^{\mathrm{C1}}\times fnit_{\mathrm{P1}}\times Tfunc \\ & \times\left\{1-\exp\left(\frac{-\alpha\times\theta^{\mathrm{C1}}\times\mathrm{PAR}}{P_{ref}^{\mathrm{C1}}\times fnit_{\mathrm{P1}}\times Tfunc}\right)\right\}\times\mathrm{C1},\end{aligned} \tag{A41}$$

$$\xi_{P1} = \xi_{NO3} \times \max\left(\frac{NP1}{PP1}, 0.5\right), \tag{A42}$$

$$NPC1 = P^{C1} - \xi_{P1} \times PP1. \tag{A43}$$

Chlorophyll uptake by picoplankton:

$$\rho_{Chl1} = \frac{\theta^{N}_{max} \times P^{C1}_{ref} \times fnit_{P1}}{\alpha \times \theta^{C1} \times PAR}. \tag{A44}$$

Nutrients uptake by diatoms:

$$NP2 = V^{C}_{N} ref_{P2} \times \frac{1 - fnit_{P2}}{1.015 - fnit_{P2}} \times Tfunc \times UNO_3S2 \times \left\{1 - \exp\left(\frac{-\alpha \times \theta^{C2} \times PAR}{P^{C2}_{ref} \times fnit_{P2} \times Tfunc}\right)\right\} \times C2, \tag{A45}$$

$$V^{C}_{N} ref_{P2} = P^{C2}_{ref} \times Q_{max}, \tag{A46}$$

$$UNO_3S2 = \min\left(\frac{NO_3}{K_{P2\_NO_3} + NO_3}, \frac{SiO_4}{K_{P2\_SiO_4} + SiO_4}\right) \times e^{-\Psi_2 NH_4}, \tag{A47}$$

$$fnit_{P2} = \frac{uQ2 - Q_{min}}{Q_{max} - Q_{min}}, \tag{A48}$$

$$uQ2 = \frac{P2}{C2}, \quad Q_{min} < uQ2 < Q_{max} \tag{A49}$$

$$\theta^{C2} = \frac{Chl2}{C2}, \tag{A50}$$

$$RP2 = V^{C}_{N} ref_{P2} \times \frac{1 - fnit_{P2}}{1.015 - fnit_{P2}} \times Tfunc \times UNH_4S2 \times \left\{1 - \exp\left(\frac{-\alpha \times \theta^{C2} \times PAR}{P^{C2}_{ref} \times fnit_{P2} \times Tfunc}\right)\right\} \times C2, \tag{A51}$$

$$UNH_4S2 = \min\left(\frac{NO_3}{K_{P2\_NO_3} + NO_3}, \frac{SiO_4}{K_{P2\_SiO_4} + SiO_4}\right) \times (1 - e^{-\Psi_2 NH_4}), \tag{A52}$$

$$PP2 = NP2 + RP2, \tag{A53}$$

$$Si2N = \frac{SiO_4/(K_{P2\_SiO_4} + SiO_4)}{NO_3/(K_{P2\_NO_3} + NO_3)}, \quad 1.0 \leqslant Si2N \leqslant 4.0, \tag{A54}$$

$$USiO_4 = V^{C}_{N} ref_{P2} \times \frac{1 - fnit_{P2}}{1.015 - fnit_{P2}} \times Tfunc \times \frac{SiO_4}{K_{P2\_SiO_4} + SiO_4} \times \left\{1 - \exp\left(\frac{-\alpha \times \theta^{C2} \times PAR}{P^{C2}_{ref} \times fnit_{P2} \times Tfunc}\right)\right\} \times C2 \times Si2N. \tag{A55}$$

Carbon uptake by diatoms:

$$P^{C2} = P^{C2}_{ref} \times fnit_{P2} \times Tfunc \times \left\{1 - \exp\left(\frac{-\alpha \times \theta^{C2} \times PAR}{P^{C2}_{ref} \times fnit_{P2} \times Tfunc}\right)\right\} \times C2, \tag{A56}$$

$$\xi_{P2} = \xi_{NO3} \times \max\left(\frac{NP2}{PP2}, 0.5\right), \tag{A57}$$

$$NPC2 = P^{C2} - \xi_{P2} \times PP2. \tag{A58}$$

Chlorophyll uptake by diatoms:

$$\rho_{Chl2} = \frac{\theta^{N}_{max} \times P^{C2}_{ref} \times fnit_{P2}}{\alpha \times \theta^{C2} \times PAR}. \tag{A59}$$

Nutrients uptake by coccolithophorids:

$$NP3 = V^{C}_{N} ref_{P3} \times \frac{1 - fnit_{P3}}{1.015 - fnit_{P3}} \times Tfunc \times \frac{NO_3}{K_{P3\_NO_3} + NO_3} \times e^{-\Psi_3 NH_4} \times \left\{1 - \exp\left(\frac{-\alpha \times \theta^{C3} \times PAR}{P^{C3}_{ref} \times fnit_{P3} \times Tfunc}\right)\right\} \times C3, \tag{A60}$$

$$V^{C}_{N} ref_{P3} = P^{C3}_{ref} \times Q_{max}, \tag{A61}$$

$$fnit_{P3} = \frac{uQ3 - Q_{min}}{Q_{max} - Q_{min}}, \tag{A62}$$

$$uQ3 = \frac{P3}{C3}, \quad Q_{min} < uQ3 < Q_{max}, \tag{A63}$$

$$\theta^{C3} = \frac{Chl3}{C3}, \tag{A64}$$

$$RP3 = V^{C}_{N} ref_{P3} \times \frac{1 - fnit_{P3}}{1.015 - fnit_{P3}} \times Tfunc \times \frac{NH_4}{K_{P3\_NH_4} + NH_4} \times \left\{1 - \exp\left(\frac{-\alpha \times \theta^{C3} \times PAR}{P^{C3}_{ref} \times fnit_{P3} \times Tfunc}\right)\right\} \times C3, \tag{A65}$$

$$PP3 = NP3 + RP3. \tag{A66}$$

Carbon uptake by coccolithophorids:

$$P^{C3} = P^{C3}_{ref} \times fnit_{P3} \times Tfunc \times \left\{1 - \exp\left(\frac{-\alpha \times \theta^{C3} \times PAR}{P^{C3}_{ref} \times fnit_{P3} \times Tfunc}\right)\right\} \times C3, \tag{A67}$$

$$\xi_{P3} = \xi_{NO3} \times \max\left(\frac{NP3}{PP3}, 0.5\right), \tag{A68}$$

$$NPC3 = P^{C3} - \xi_{P3} \times PP3. \tag{A69}$$

Chlorophyll uptake by coccolithophorids:

$$\rho_{Chl3} = \frac{\theta^{N}_{max} \times P^{C3}_{ref} \times fnit_{P3}}{\alpha \times \theta^{C3} \times PAR}. \tag{A70}$$

Grazing on picoplankton and bacteria by microzooplankton:

$$G_1 = G1_{max} \frac{\zeta_5 P1}{K1_{gr} + \zeta_5 P1 + \zeta_6 BAC} Z1, \tag{A71}$$

$$G_6 = G1_{max} \frac{\zeta_6 BAC}{K1_{gr} + \zeta_5 P1 + \zeta_6 BAC} Z1, \tag{A72}$$

$$\zeta_5 = \frac{\rho_5 P1}{\rho_5 P1 + \rho_6 BAC}, \tag{A73}$$

$$\zeta_6 = \frac{\rho_6 BAC}{\rho_5 P1 + \rho_6 BAC}. \tag{A74}$$

Grazing on diatoms, microzooplankton, detritus and coccolithophorids by mesozooplankton:

$$G_2 = G2_{max} \frac{\zeta_1 P2}{K2_{gr} + \zeta_1 P2 + \zeta_2 Z1 + \zeta_3 PON + \zeta_4 P3} Z2, \tag{A75}$$

$$G_3 = G2_{\max}\frac{\zeta_2 Z1}{K2_{gr} + \zeta_1 P2 + \zeta_2 Z1 + \zeta_3 PON + \zeta_4 P3} Z2, \quad (A76)$$

$$G_4 = G2_{\max}\frac{\zeta_3 PON}{K2_{gr} + \zeta_1 P2 + \zeta_2 Z1 + \zeta_3 PON + \zeta_4 P3} Z2, \quad (A77)$$

$$G_5 = G2_{\max}\frac{\zeta_4 P3}{K2_{gr} + \zeta_1 P2 + \zeta_2 Z1 + \zeta_3 PON + \zeta_4 P3} Z2, \quad (A78)$$

$$\zeta_1 = \frac{\rho_1 P2}{\rho_1 P2 + \rho_2 Z1 + \rho_3 PON + \rho_4 P3}, \quad (A79)$$

$$\zeta_2 = \frac{\rho_2 Z1}{\rho_1 P2 + \rho_2 Z1 + \rho_3 PON + \rho_4 P3}, \quad (A80)$$

$$\zeta_3 = \frac{\rho_3 PON}{\rho_1 P2 + \rho_2 Z1 + \rho_3 PON + \rho_4 P3}, \quad (A81)$$

$$\zeta_4 = \frac{\rho_4 P3}{\rho_1 P2 + \rho_2 Z1 + \rho_3 PON + \rho_4 P3}. \quad (A82)$$

Bacteria uptake of LDOM (Anderson and Williams, 1998):

$$U_C = \mu B_{\max} \times R_B \frac{LDOC}{K_L + LDOC} BAC, \quad (A83)$$

$$U_N = U_C \frac{LDON}{LDOC}. \quad (A84)$$

Bacteria uptake of ammonia, DOM, respiration, and ammonia remineralization:

$$U_B^* = \mu B_{\max} \times BAC \frac{NH_4}{K_B + NH_4}. \quad (A85)$$

(1) If ammonium uptake is sufficient to permit utilization of DOM, that is, $U_B^* \geqslant -U_C\left(\frac{U_N}{U_C} - \frac{(1-r\_b)}{R_B}\right)$, then bacteria uptake of DOM has the form of

$$F_B = (1 - r\_b)\frac{U_C}{R_B}, \quad (A86)$$

bacteria respiration,

$$S_B = r\_b \times U_C, \quad (A87)$$

remineralization by bacteria,

$$E_B = U_C\left(\frac{U_N}{U_C} - \frac{(1 - r\_b)}{R_B}\right). \quad (A88)$$

If $E_B > 0$, then $U_B = 0$; otherwise, $U_B = -E_B$.

(2) If there is insufficient ammonium, that is, $U_B^* < -U_C\left(\frac{U_N}{U_C} - \frac{(1-r\_b)}{R_B}\right)$, then bacteria uptake of ammonia is obtained by,

$$U_B = U_B^*, \quad (A89)$$

bacteria uptake of DOM,

$$F_B = U_N + U_B, \quad (A90)$$

bacteria respiration,

$$S_B = R_B F_B \frac{r\_b}{1 - r\_b}, \quad (A91)$$

remineralization by bacteria,

$$E_B = -U_B. \quad (A92)$$

CDOM photolysis (Bissett et al., 1999a):

$$UVLDOC = a_{CLDOC}(410) \times RtUVLDOC \times \left(\frac{PAR(0)}{410}\right) \times \exp\left[\int_z^0 Kd(300)dz\right], \quad (A93)$$

$$UVSDOC = a_{CSDOC}(410) \times RtUVSDOC \times \left(\frac{PAR(0)}{410}\right) \times \exp\left[\int_z^0 Kd(300)dz\right], \quad (A94)$$

$$UVLDIC = a_{CLDOC}(410) \times RtUVLDIC \times \left(\frac{PAR(0)}{410}\right) \times \exp\left[\int_z^0 Kd(300)dz\right], \quad (A95)$$

$$UVSDIC = a_{CSDOC}(410) \times RtUVSDIC \times \left(\frac{PAR(0)}{410}\right) \times \exp\left[\int_z^0 Kd(300)dz\right], \quad (A96)$$

$$a_{CLDOC}(410) = a^*_{cdoc} \times CLDOC, \quad (A97)$$

$$a_{CSDOC}(410) = a^*_{cdoc} \times CSDOC, \quad (A98)$$

$$Kd(300) = [a_{CLDOC}(410) + a_{CSDOC}(410)] \times \exp[0.0145 \times (410 - 300)] + 0.154. \quad (A99)$$

The dissolution rate for biogenic silica (Jiang et al., 2003):

$$D_{Si} = (0.19T/25 + 0.01) \times \exp(0.069(T - 25)). \quad (A100)$$

The air–sea flux of CO_2 is calculated using the transfer velocity-wind speed relationships from Wanninkhof (1992):

$$air - sea\ CO_2\ flux = 0.31U^2(660/Sc)^{0.5}S\{(pCO_2)_{sea} - (pCO_2)_{air}\}, \quad (A101)$$

where U is the wind speed at sea surface and Sc is the Schmidt number for CO_2 that can be calculated as:

$$Sc = 2073.1 - 125.62T + 3.6276T^2 - 0.043219T^3, \quad (A102)$$

S is the solubility of CO_2 and $(pCO_2)_{air}$ is the partial pressure of CO_2 in the air. In the model, we set a spatially uniform distribution of $(pCO_2)_{air}$ observed at the Mauna Loa Observatory (Keeling et al., 1976).

Dissolved oxygen (DO) is modeled using constant oxygen-to-nitrate and oxygen-to-ammonium ratios. At the surface, air-sea exchange of O_2 is calculated as:

$$O_2\ flux = 0.31U^2(660/So2)^{0.5}(DO_{sat} - DO), \quad (A103)$$

where DO_{sat} is the saturation concentration of DO calculated from temperature and salinity. So2 is the Schmidt number for O_2 that can be calculated as follows:

$$So2 = 1638.0 - 81.83T + 1.483T^2 - 0.008004T^3. \quad (A104)$$

References

Anderson, T.R., Williams, P.J.B., 1998. Modelling the seasonal cycle of dissolved organic carbon at station E1 in the English Channel. Estuarine, Coastal and Shelf Science 46, 93–109.

Anderson, T.R., Pondaven, P., 2003. Non-redfield carbon and nitrogen cycling in the Sargasso Sea: pelagic imbalances and export flux. Deep Sea Research 50, 573–591.

Aumont, O., Maier-Reimer, E., Blain, S., Monfray, P., 2003. An ecosystem model of the global ocean including Fe, Si, P co-limitation. Global Biogeochem. Cycles 17 (2), 1060. http://dx.doi.org/10.1029/2001GB001745.

Babin, M., Stramski, D., Ferrari, G.M., Claustre, H., Bricaud, A., Obolensky, G., Hoepffner, N., 2003a. Variations in the light absorption coefficients of phytoplankton, non-algal particles, and dissolved organic matter in coastal waters around Europe. Journal of Geophysical Research. http://dx.doi.org/10.1029/2001JC000882.

Babin, M., Morel, A., Fournier-Sicre, V., Fell, F., Stramski, D., 2003b. Light scattering properties of marine particles in coastal and open ocean waters as related to the particle mass concentration. Limnology and Oceanography 48 (2), 843–859.

Balch, W.M., Kilpatrick, K.A., Holligan, P., Harbour, D., Fernandez, E., 1996. The 1991 coccolithophore bloom in the central North Atlantic. 2. Relating optics to coccolith concentration. Limnology and Oceanography 41 (8), 1684–1696.

Behrenfeld, M.J., Falkowski, P.G., 1997. Photosynthetic rates derived from satellite-based chlorophyll concentration. Limnology and Oceanography 42, 1–20.

Behrenfeld, M.J., Boss, E., Siegel, D.A., Shea, D.M., 2005. Carbon-based ocean productivity and phytoplankton physiology from space. Global Biogeochemical Cycles 19, GB1006. http://dx.doi.org/10.1029/2004GB002299.

Bissett, W.P., Carder, K.L., Walsh, J.J., Dieterle, D.A., 1999a. Carbon cycling in the upper waters of the Sargasso Sea: II. Numerical simulation of apparent and inherent optical properties. Deep Sea Research: I 46, 271–317.

Bissett, W.P., Walsh, J.J., Dieterle, D.A., Carder, K.L., 1999b. Carbon cycling in the upper waters of the Sargasso Sea: I. Numerical simulation of differential carbon and nitrogen fluxes. Deep Sea Research I 46, 205–269.

Bissett, W.P., Schofield, O., Glenn, S., Cullen, J.J., Miller, W.L., Plueddemann, A.J., Mobley, C.D., 2001. Resolving the impacts and feedback of ocean optics on upper ocean ecology. Oceanography 14 (3), 30–53.

Bissett, W.P., DeBra, S., Dye, D., 2004. Ecological Simulation (EcoSim) 2.0 Technical Description. FERI Tech. Doc. Num. FERI-2004-0002-U-D, August 10, 2004. Tampa, Fl, 27 pp.

Boss, E., Stramski, D., Bergmann, T., Pegau, W.S., Lewis, M., 2004. Why should we measure the optical backscattering coefficient? Oceanography 17 (2), 44–49.

Bricaud, A., Morel, A., Prieur, L., 1983. Optical efficiency factors of some phytoplankters. Limnology and Oceanography 28, 816–832.

Carder, K.L., Steward, R.G., Harvey, G.R., Ortner, P.B., 1989. Marine humic and fulvic acids: their effects on remote sensing of ocean chlorophyll. Limnology and Oceanography 34 (1), 68–81.

Chai, F., Dugdale, R.C., Peng, T.-H., Wilkerson, F.P., Barber, R.T., 2002. One dimensional ecosystem model of the Equatorial Pacific upwelling system. Part I: Model development and silicon and nitrogen cycle. Deep Sea Research: II 49, 2713–2745.

Christian, J.R., Anderson, T.R., 2002. Modeling DOM biogeochemistry. In: Hansell, D.A., Carlson, C.A. (Eds.), Biogeochemistry of Marine Dissolved Organic Matter. Academic Press, pp. 717–756.

Coale, K.H., Johnson, K.S., Fitzwater, S.E., Gordon, R.M., Tanner, S., Chavez, F.P., Ferioli, L., Sakamoto, C., Rogers, P., Millero, F., Steinberg, P., Nightingale, P., Cooper, D., Cochlan, W.P., Landry, M.R., Constantinou, J., Rollwagen, G., Trasvina, A., Kudela, R., 1996. A massive phytoplankton bloom induced by an ecosystem-scale iron fertilization experiment in the equatorial Pacific Ocean. Nature 383, 495–501.

Dore, J.E., Letelier, R.M., Church, M.J., Lukas, R., Karl, D.M., 2008. Summer phytoplankton blooms in the oligotrophic North Pacific Subtropical Gyre: historical perspective and recent observations. Progress in Oceanography 76, 2–38.

DuRand, M.D., Olson, R.J., Chisholm, S.W., 2001. Phytoplankton population dynamics at the Bermuda Atlantic Time-series station in the Sargasso Sea. Deep Sea Research: II 48, 1983–2003.

Eppley, R.W., Chavez, F.P., Barber, R.T., 1992. Standing stocks of particulate carbon and nitrogen in the Equatorial Pacific at 150°W. Journal of Geophysical Research 97, 655–661.

Fennel, K., Abbott, M.R., Spitz, Y.H., Richman, J.G., Nelson, D.M., 2003. Modeling controls of phytoplankton production in the southwest Pacific sector of the Southern Ocean. Deep-Sea Research II 50, 769–798.

Fujii, M., Boss, E., Chai, F., 2007. The value of adding optics to ecosystem models: a case study. Biogeosciences 4, 817–835.

Fujii, M., Chai, F., 2007. Modeling carbon and silicon cycling in the equatorial Pacific. Deep Sea Research II 54, 496–520.

Garcia, H.E., Locarnini, R.A., Boyer, T.P., Antonov, J.I., 2006. World Ocean Atlas 2005. In: Levitus, S. (Ed.), Nutrients Phosphate Nitrate Silicate. Atlas NESDIS 64, vol. 4. U.S. Government Printing Office, Washington, DC.

Geider, R.J., Macintyre, H.L., Kana, T.M., 1998. A dynamic regulatory model of phytoplanktonic acclimation to light, nutrients, and temperature. Limnology and Oceanography 43, 679–694.

Goebel, N.L., Edwards, C.A., Zehr, J.P., Follows, M.J., 2010. An emergent community ecosystem model applied to the California Current System. Journal of Marine System 83, 221–241.

Gordon, H.R., Boynton, G.C., Balch, W.M., Groom, S.B., Harbour, D.S., Smyth, T.J., 2001. Retrieval of coccolithophore calcite concentration from SeaWiFS imagery. Geophysical Research Letters 28, 1587–1590.

IOCCG, 2000. Remote sensing of ocean color in coastal, and other optically complex waters. In: Sathyendranath, S. (Ed.), Reports of the International Ocean-Colour Coordinating Group, No. 3, Dartmouth, Canada.

IOCCG, 2006. Remote sensing of inherent optical properties: fundamentals, test of algorithms, and applications. In: Lee, Z.-P. (Ed.), Reports of the International Ocean-Colour Coordinating Group, No. 5, Dartmouth, Canada.

Jiang, M.-S., Chai, F., Barber, R.T., Dugdale, R.C., Wilkerson, F., Peng, T.-H., 2003. A nitrate and silicate budget in the Equatorial Pacific Ocean: a coupled biological-physical model study. Deep Sea Research: II 50, 2971–2996.

Kalnay, E., Kanamitsu, M., Kistler, R., Collins, W., Deaven, D., Gandin, L., Iredell, M., Saha, S., White, G., Woollen, J., Zhu, Y., Chelliah, M., Ebisuzaki, W., Higgins, W., Janowiak, J., Mo, K.C., Ropelewski, C., Wang, J., Jenne, R., Joseph, D., 1996. The NCEP/NCAR 40-year reanalysis project. Bulletin of the American Meteorological Society 77, 437–471.

Keeling, C.D., Bacastow, R.B., Bainbridge, A.E., Ekdahl, C.A., Guenther, P.R., Waterman, L.S., 1976. Atmospheric carbon dioxide variations at Mauna Loa Observatory, Hawaii. Tellus 28, 538–551.

Key, R.M., Kozyr, A., Sabine, C.L., Lee, K., Wanninkhof, R., Bullister, J., Feely, R.A., Millero, F., Mordy, C., Peng, T.-H., 2004. A global ocean carbon climatology: results from GLODAP. Global Biogeochemical Cycles 18, GB4031.

Kishi, M.J., Kashiwai, M., Ware, D.M., Megrey, B.A., Eslinger, D.L., Werner, F.E., Noguchi-Aita, M., Azumaya, T., Fujii, M., Hashimoto, S., Huang, D., Iizumi, H., Ishida, Y., Kang, S., Kantakov, G.A., Kim, H., Komatsu, K., Navrotsky, V.V., Smith, S.L., Tadokoro, K., Tsuda, A., Yamamura, O., Yamanaka, Y., Yokouchi, K., Yoshie, N., Zhang, J., Zuenko, Y.I., Zvalinsky, V.I., 2007. NEMURO—a lower trophic level model for the North Pacific marine ecosystem. Ecological Modellling 202, 12–25.

Large, W.G., Pond, S., 1982. Sensible and latent heat flux measurements over the ocean. Journal of Physical Oceanography 12, 464–482.

Lee, Z.P., Carder, K.L., Arnone, R.A., 2002. Deriving inherent optical properties from water color: a multi-band quasi-analytical algorithm for optically deep waters. Applied Optics 41, 5755–5772.

Lee, Z., Du, K., Arnone, R., Liew, S., Penta, B., 2005. Penetration of solar radiation in the upper ocean: a numerical model for oceanic and coastal waters. Journal of Geophysical Research 110, C09019. http://dx.doi.org/10.1029/2004JC002780.

Levy, M., Memery, L., Andre, J.-M., 1998. Simulation of primary production and export fluxes in the Northwestern Mediterranean Sea. Journal of Marine Research 56, 197–238.

Locarnini, R.A., Mishonov, A.V., Antonov, J.I., Boyer, T.P., Garcia, H.E., 2006. World Ocean Atlas 2005. In: Levitus, S. (Ed.), Temperature, NOAA Atlas NESDIS 61, vol. 1. U.S. Government Printing Office, Washington, DC.

Martin, J.H., Coale, K.H., Johnson, K.S., Fitzwater, S.E., Gordon, R.M., Tanner, S.J., Hunter, C.N., Elrod, V.A., Nowicki, J.L., Coley, T.L., Barber, R.T., Lindley, S., Watson, A.J., van Scoy, K., Law, C.S., Liddicoat, M.I., Ling, R., Stanton, T., Stockel, J., Collins, C., Anderson, A., Bidigare, R., Ondrusek, M., Latasa, M., Millero, F.J., Lee, K., Yao, W., Zhang, J.Z., Friederich, G., Sakamoto, C., Chavez, F., Buck, K., Kolber, Z., Greene, R., Falkowski, P., Chisholm, S.W., Hoge, F., Swift, R., Yungel, J., Turner, S., Nightingale, P., Hatton, A., Liss, P., Tindale, N.W., 1994. Testing the iron hypothesis in ecosystems of the equatorial Pacific Ocean. Nature 371, 123–129.

Millan-Nuñez, R., Alvarez-Borrego, S., Trees, C.C., 1996. Relationship between deep chlorophyll maximum and surface chlorophyll concentration in the California Current System. CalCOFI Report, 37.

Moore, J.K., Doney, S.C., Kleypas, J.A., Glover, D.M., Fung, I.Y., 2002. An intermediate complexity marine ecosystem model for the global domain. Deep Sea Research: II 49, 403–462.

Morel, A., 1974. Optical properties of pure water and pure seawater. In: Jerlov, E., Steeman Nielsen (Eds.), Optical Aspects of Oceanography. Academic Press, New York, pp. 1–24.

Nanninga, H.J., Tyrrell, T., 1996. Importance of light for the formation of algal blooms by *Emiliania huxleyi*. Marine Ecology Progress Series 136, 195–203.

Nelson, N.B., Siegel, D.A., 2013. The global distribution and dynamics of chromophoric dissolved organic matter. Annual Review of Marine Science 5, 447–476.

Pope, R.M., Fry, E.S., 1997. Absorption spectrum (380–700 nm) of pure water. II. Integrating cavity measurements. Applied Optics 36, 8710–8723.

Ragueneau, O., Treguer, P., Leynaert, A., Anderson, R.F., Brzezinski, M.A., Demaster, D.J., Dugdale, R.C., Dymond, J., Fischer, G., Francois, R., Heinze, C., Maier-Reimer, E., Martin-Jezequel, V., Nelson, N.B., Queguiner, B., 2000. A review of the Si cycle in the modern ocean: recent progress and missing gaps in the application of biogenic opal as a paleoproductivity proxy. Global and Planetary Change 26, 317–365.

Rothstein, L.M., Cullen, J.J., Abbott, M., Chassignet, E.P., Denman, K., Doney, S.C., Ducklow, H., Fennel, K., Follows, M., Haidvogel, D., Hoffman, E., Karl, D.M., Kindle, J., Lima, I., Maltrud, M., McClain, C., McGillicuddy, D., Olascoaga, M.J., Spitz, Y., Wiggert, J., Yoder, J., 2006. Modeling ocean ecosystems: the PARADIGM program. Oceanography 19 (1), 22–51.

Shchepetkin, A.F., McWilliams, J.C., 2005. The regional ocean modeling system: a split-explicit, free-surface, topography following coordinates ocean model. Ocean Modelling 9, 347–404.

Shulman, I., Frolov, S., Anderson, S., Penta, B., Gould, R., Sakalaukus, P., Ladner, S., 2013. Impact of bio-optical data assimilation on short-term coupled physical, bio-optical model predictions. Journal of Geophysical Research Oceans 118. http://dx.doi.org/10.1002/jgrc.20177.

Siegel, D.A., Maritorena, S., Nelson, N.B., Behrenfeld, M.J., McClain, C.R., 2005. Colored dissolved organic matter and its influence on the satellite-based characterization of the ocean biosphere. Geophysical Research Letters 32, L20605. http://dx.doi.org/10.1029/2005GL024310.

Smith, R.C., Baker, K.S., 1978. The bio-optical state of ocean waters and remote sensing. Limnology and Oceanography 23, 247–259.

Stramski, D., Reynolds, R.A., Kahzu, M., Mitchell, B.G., 1999. Estimation of particulate organic carbon in the ocean from satellite remote sensing. Science 285 (5433), 239–242.

Strom, S.L., Benner, R., Ziegler, S., Dagg, M.J., 1997. Planktonic grazers are a potentially important source of marine dissolved organic carbon. Limnology and Oceanography 42, 1364–1374.

Sumata, H., Hashioka, T., Suzuki, T., Yoshie, N., Okunishi, T., Aita, M.N., Sakamoto, T.T., Ishida, A., Okada, N., Yamanaka, Y., 2010. Effect of eddy transport on the nutrient supply into the euphotic zone simulated in an eddy-permitting ocean ecosystem model. Journal of Marine System 83, 67–87.

Swan, C.M., Siegel, D.A., Nelson, N.B., Carlson, C.A., Nasir, E., 2009. Biogeochemical and hydrographic controls on chromophoric dissolved organic matter distribution in the Pacific Ocean. Deep Sea Research: I 56, 2175–2192.

Tian, R.C., Vézina, A.F., Legendre, L., Ingram, R.G., Klein, B., Packard, T., Roy, S., Savenkoff, C., Silverberg, N., Therriault, J.-C., Tremblay, J.-E., 2000. Effects of pelagic food-web interactions and nutrient remineralization on the biogeochemical cycling of carbon: a modeling approach. Deep Sea Research: II 47, 637–662.

Vallino, J.J., 2000. Improving marine ecosystem models: use of data assimilation and mesocosm experiments. Journal of Marine Research 58, 117–164.

Volkman, J.K., Tanoue, E., 2002. Chemical and biological studies of particulate organic matter in the ocean. Journal of Oceanography 58, 265–279.

Walsh, J.J., Dieterle, A.D., Muller-Karger, F.E., Bohrer, R., Bissett, W.P., Varela, R.J., Aparicio, R., Diaz, R., Thunell, R., Taylor, G.T., Scranton, M.I., Fanning, K.A., Peltzer, E.T., 1999. Simulation of carbon–nitrogen cycling during spring upwelling in the Cariaco Basin. Journal of Geophysical Research 104 (C4), 7807–7825.

Wanninkhof, R., 1992. Relationship between wind speed and gas exchange over the ocean. Journal of Geophysical Research 97, 7373–7382.

Ward, B.B., 2000. Nitrification and the marine nitrogen cycle. In: Kirchman, D.L. (Ed.), Microbial Ecology of the Oceans. Wiley, New York, pp. 427–453.

Werdell, P.J., Bailey, S.W., 2002. The SeaWiFS Bio-optical Archive and Storage System (SeaBASS): current architecture and implementation. In: Fargion, G.S., McClain, C.R. (Eds.), NASA Tech. Memo. 2002-211617, NASA Goddard Space Flight Center, Greenbelt, Maryland, 45 pp.

Wetzel, R.G., Hatcher, P.G., Bianchi, T.S., 1995. Natural photolysis by ultraviolet irradiance or recalcitrant dissolved organic matter to simple substrates for rapid bacterial metabolism. Limnology and Oceanography 40 (8), 1369–1380.

Xiu, P., Chai, F., 2012. Spatial and temporal variability in phytoplankton carbon, chlorophyll, and nitrogen in the North Pacific. Journal of Geophysical Research 117, C11023. http://dx.doi.org/10.1029/2012JC008067.

Yamanaka, Y., Yoshie, N., Fujii, M., Aita, M.N., Kishi, M., 2004. An ecosystem model coupled with nitrogen–silicon–carbon cycles applied to Station A7 in the northwestern Pacific. Journal of Oceanography 60, 227–241.

Yamashita, Y., Tanoue, E., 2009. Basin scale distribution of chromophoric dissolved organic matter in the Pacific Ocean. Limnology and Oceanography 54, 598–609.

Yentsch, C.S., Phinney, D.A., 1989. A bridge between ocean optics and microbial ecology. Limnology and Oceanography 34, 1694–1705.

Zepp, R.G., Schlotzhauer, P.F., 1981. Comparison of photochemical behavior of various humic substances in water: III. Spectroscopic properties of humic substances. Chemosphere 10 (5), 479–486.